

On the role of AGN feedback on the thermal and chemodynamical properties of the hot intra-cluster medium

S. Planelles^{1,2*}, S. Borgani^{1,2,3}, D. Fabjan^{3,6,7}, M. Killedar^{1,2}, G. Murante²,
G. L. Granato², C. Ragonè-Figueroa^{8,2}, K. Dolag^{4,5}

¹ *Astronomy Unit, Department of Physics, University of Trieste, via Tiepolo 11, I-34131 Trieste, Italy*

² *INAF, Osservatorio Astronomico di Trieste, via Tiepolo 11, I-34131 Trieste, Italy*

³ *INFN – National Institute for Nuclear Physics, Via Valerio 2, I-34127 Trieste, Italy*

⁴ *Universitätssternwarte München, Scheinerstr. 1, D-81679 München, Germany*

⁵ *Max-Planck-Institut für Astrophysik, P.O. Box 1317, D-85741 Garching, Germany*

⁶ *SPACE-SI, Slovenian Centre of Excellence for Space Sciences and Technologies, Aškerčeva 12, 1000 Ljubljana, Slovenia*

⁷ *Faculty of Mathematics and Physics, University of Ljubljana, Jadranska 19, 1000 Ljubljana, Slovenia*

⁸ *Instituto de Astronomía Teórica y Experimental (IATE),*

Consejo Nacional de Investigaciones Científicas y Técnicas de la República Argentina (CONICET),

Observatorio Astronómico, Universidad Nacional de Córdoba, Laprida 854, X5000BGR, Córdoba, Argentina

24 September 2018

ABSTRACT

We present an analysis of the properties of the intra-cluster medium (ICM) in an extended set of cosmological hydrodynamical simulations of galaxy clusters and groups performed with the TreePM+SPH GADGET–3 code. Besides a set of non-radiative simulations, we carried out two sets of simulations including radiative cooling, star formation, metal enrichment and feedback from supernovae (SNe), one of which also accounts for the effect of feedback from active galactic nuclei (AGN) resulting from gas accretion onto super-massive black holes. These simulations are analysed with the aim of studying the relative role played by SN and AGN feedback on the general properties of the diffuse hot baryons in galaxy clusters and groups: scaling relations, temperature, entropy and pressure radial profiles, and ICM chemical enrichment. We find that simulations including AGN feedback produce scaling relations between X-ray observable quantities that are in good agreement with observations at all mass scales. Observed pressure profiles are also shown to be quite well reproduced in our radiative simulations, especially when AGN feedback is included. However, our simulations are not able to account for the observed diversity between cool-core and non cool-core clusters, as revealed by X-ray observations: unlike for observations, we find that temperature and entropy profiles of relaxed and unrelaxed clusters are quite similar and resemble more the observed behaviour of non cool-core clusters. As for the pattern of metal enrichment, we find that an enhanced level of iron abundance is produced by AGN feedback with respect to the case of purely SN feedback. As a result, while simulations including AGN produce values of iron abundance in groups in agreement with observations, they over-enrich the ICM in massive clusters. The efficiency of AGN feedback in displacing enriched gas from halos into the intergalactic medium at high redshift also creates a widespread enrichment in the outskirts of clusters and produces profiles of iron abundance whose slope is in better agreement with observations. By analysing the pattern of the relative abundances of silicon and iron and the fraction of metals in the stellar phase, our results clearly show that different sources of energy feedback leave different imprints in the enrichment pattern of the hot ICM and stars. Our results confirm that including AGN feedback goes in the right direction of reconciling simulation predictions and observations for several observational ICM properties. Still a number of important discrepancies highlight that the model still needs to be improved to produce the correct interplay between cooling and feedback in central cluster regions.

Key words: cosmology: miscellaneous – methods: numerical – galaxies: cluster: general – X-ray: galaxies.

1 INTRODUCTION

The sensitivity reached by X-ray observations with the current generation of soft X-ray telescopes (*Chandra*, *XMM-Newton* and *SUZAKU*) has provided us with a detailed analysis of the thermo- and chemodynamical properties of the hot intra-cluster medium (ICM) for statistically representative samples of galaxy clusters. These observations have now established some of the main ICM properties: temperature profiles have negative gradients outside core regions out to the largest radii covered so far by observations (e.g., De Grandi and Molendi 2002; Vikhlinin et al. 2005; Zhang et al. 2006; Baldi et al. 2007; Pratt et al. 2007; Leccardi and Molendi 2008a); gas entropy in poor clusters and groups is higher than expected from simple self-similar scaling relations of the ICM (see Giodini et al. 2013, for a recent review on observational scaling relations and references therein); radial profiles of the iron abundance show negative gradients, more pronounced for relaxed cool-core (CC) clusters, with central values of Z_{Fe} approaching the solar abundance and with a global enrichment at a level of about $1/3$ – $1/2$ $Z_{\text{Fe},\odot}$ (De Grandi et al. 2004; Vikhlinin et al. 2005; de Plaa et al. 2006; Snowden et al. 2008; Leccardi and Molendi 2008a; Werner et al. 2008); relaxed clusters also show core regions with very low amounts of gas cooler than about one third of their virial temperature (e.g., Peterson et al. 2001; Böhringer et al. 2002; Sanderson et al. 2006); etc.

Complementary to X-ray observations, clusters observed in large Sunyaev-Zel'dovich (SZ) surveys offer an additional channel to analyze the properties of the hot ICM (see Carlstrom et al. 2002, for a review). While the X-ray signal is proportional to the square of the gas density, the SZ effect (Sunyaev and Zeldovich 1972) depends on the integrated pressure along the line of sight, which decreases more gently with radius (e.g., Arnaud et al. 2010). It is thanks to the larger dynamic range in gas density accessible and the redshift independence of the signal that SZ observations are the ideal complement to X-ray observations. New generations of millimetre instruments are now routinely detecting the SZ signal of galaxy clusters, sometimes out to large radii, thereby opening a new window on the study of the thermodynamics of the hot baryons in galaxy clusters (e.g., Planck Collaboration et al. 2013; Reichardt et al. 2013; Hasselfield et al. 2013; Plagge et al. 2013).

Given the range of scales involved by galaxy clusters, their observational properties arise from a non-trivial interplay between gravitational processes, which shape the large-scale structure of the Universe, and a number of astrophysical processes that take place on much smaller scales (e.g., radiative cooling, star formation and its associated energy and chemical feedback and AGN heating). Within this context, it is only with cosmological hydrodynamical simulations that one can capture the full complexity of the problem (see Borgani and Kravtsov 2009; Kravtsov and Borgani 2012, for recent reviews). In the last two decades much progress has been made in the numerical modelling of the formation and evolution of galaxy clusters and groups, thanks to the ever evolving efficiency of sophisticated cosmological hydrodynamical simulation codes, that include now advanced descriptions of the astrophysical processes shaping galaxy formation, and the rapid increase of accessible supercomputing power (e.g., Evrard 1990; Navarro et al. 1995; Bryan and Norman 1998; Kravtsov and Yepes 2000; Borgani et al. 2001; Springel et al. 2001; Kay et al. 2002).

These simulations have had varying degrees of success in reproducing the thermodynamical properties of the hot ICM. It is well established that simulations that include only the effects of radiative cooling form too many stars relative to observational re-

sults (see Balogh et al. 2001, for further discussion of this ‘cooling crisis’). The solution to this problem should be provided by a suitable mechanism combining the action of heating and cooling processes in a self-regulated way (e.g. Voit 2005, for a review). Different forms of energy feedback from supernova (SN) explosions have been proposed to generate a self-regulated star formation (Springel and Hernquist 2003). However, models based on the action of stellar feedback are not able to regulate star formation to the low levels observed in the most massive galaxies hosted at the centre of rich galaxy clusters, the so-called brightest cluster galaxies (BCGs; e.g. Borgani et al. 2004 and references therein). Within this scenario, it is becoming increasingly clear that AGN feedback is the most plausible source of heating to counteract gas cooling within the massive DM halos of groups and clusters. It is only relatively recently that studies of the effect of AGN feedback in cosmological simulations of galaxy clusters have been undertaken by a number of independent groups (e.g., Sijacki et al. 2007; Puchwein et al. 2008; McCarthy et al. 2010; Puchwein et al. 2010; Fabjan et al. 2010; Short et al. 2010; Battaglia et al. 2012b; Dubois et al. 2011; Martizzi et al. 2012). Due to its central location and its ability to provide enough energy, a growing number of authors have argued that gas accretion onto supermassive black holes (SMBHs) plays a crucial role in regulating the star formation rates of massive galaxies (e.g., Granato et al. 2004; Springel et al. 2005; Bower et al. 2006, 2008) and suppressing overcooling in groups and clusters (e.g., Churazov et al. 2001), a picture that is broadly supported by a large body of observational evidence (e.g. McNamara and Nulsen 2007, for a review).

Motivated by this idea, Springel et al. (2005) developed a novel scheme to follow the growth of supermassive BHs and the ensuing feedback from AGN in cosmological smoothed particle hydrodynamics (SPH) simulations (see also Sijacki and Springel 2006; Booth and Schaye 2009, for subsequent modifications of this model). Using this original implementation of AGN feedback as a reference, Sijacki and Springel (2006), Sijacki et al. (2007), Puchwein et al. (2008), Bhattacharya et al. (2008) and Fabjan et al. (2010) went one step further and modified the original implementation to include both ‘quasar’ and ‘radio’ feedback modes. The former is characterised by isotropic thermal heating of the gas when accretion rates are high, while the latter, characteristic when accretion rates are low, consists of thermal heating meant to mimic ‘bubbles’ observed in many nearby clusters, which are thought to be inflated by relativistic jets coming from the central BH¹. As for Eulerian adaptive mesh refinement (AMR) simulations, an alternative way of implementing the AGN energy injection is through AGN-driven winds, which shock and heat the surrounding gas (e.g., Dubois et al. 2011; Gaspari et al. 2011; Martizzi et al. 2012; see also Barai et al. 2013 for an SPH implementation of kinetic AGN feedback).

As a result of these analyses, AGN feedback was generally found to yield reduced stellar mass fractions and star formation rates in a cosmological context, while reproducing better a number of observable properties of the ICM (see also McCarthy et al. 2010). For example, Puchwein et al. (2008) found that including energy input from supermassive BHs enables their simulations to reproduce the luminosity-temperature and gas mass fraction-

¹ Only the models by Sijacki and Springel (2006) and Sijacki et al. (2007) were explicitly modified to include the possibility to inflate high-entropy bubbles in the ICM whenever accretion onto the central BH enters in a quiescent ‘radio’ mode.

temperature relations of groups and clusters. Fabjan et al. (2010) found similarly good matches to these relations, while also showing that their simulations yielded temperature profiles in reasonable agreement with observations of galaxy groups.

Less attention has been paid so far to analyze the interplay between AGN and chemical enrichment by including a detailed chemodynamical description of the ICM (e.g., Sijacki et al. 2007; Moll et al. 2007; Fabjan et al. 2010; McCarthy et al. 2010). Measurements of the enrichment pattern of the ICM represent a unique means towards a unified description of the thermodynamical properties of the diffuse gas and of the past history of star formation within the population of cluster galaxies (e.g., Renzini et al. 1993; Borgani et al. 2008). In fact, recent analyses of the ICM metal enrichment from cosmological simulations including the effect of AGN feedback show that this mechanism can actually displace a large amount of highly-enriched gas that is already present inside massive halos at the redshift $z \sim 2-3$, at which SMBH accretion peaks. The resulting widespread enrichment of the intergalactic medium leads to a sensitive change of the amount and distribution of metals within clusters and groups at low redshift (e.g., Fabjan et al. 2010; McCarthy et al. 2011).

The aim of this paper is to present a detailed analysis of the properties of the ICM for an extended set of cosmological hydrodynamical simulations of galaxy clusters, which have been performed with the TreePM+SPH GADGET-3 code (Springel 2005). We carried out one set of non-radiative simulations, and two sets of simulations including metallicity-dependent radiative cooling, star formation, metal enrichment and feedback from supernovae, one of which also accounts for the effect of an efficient model of AGN feedback. The scheme of AGN feedback implemented in these simulations is a modification of the original model presented in Fabjan et al. (2010) with some improvements related, especially, to the way in which BHs are seeded and are allowed to grow, with their positioning within their host galaxy and with the way in which the thermal energy is distributed. We will show results on the effect that the different feedback mechanisms implemented in our simulations have on the ICM thermodynamical properties of our systems and on the corresponding pattern of chemical enrichment.

The paper is organized as follows: in Section 2, we describe our set of simulated galaxy clusters, the numerical implementation of the different physical processes included in our simulations, and the definitions of the observable quantities computed from the simulations. In Section 3 we present the results obtained from this set of simulations on general X-ray properties of the ICM and we compare them with different observational results. Section 4 is devoted to the description of the metal enrichment of the ICM in our simulations. Finally, we discuss our results and summarise our main conclusions in Section 5.

2 THE SIMULATED CLUSTERS

2.1 Initial conditions

Our sample of simulated clusters and groups are obtained from 29 Lagrangian regions, centred around as many massive halos identified within a large-volume, low-resolution N-body cosmological simulation (see Bonafede et al. 2011, for details). The cosmological model assumed is a flat Λ CDM one, with $\Omega_m = 0.24$ for the matter density parameter, $\Omega_b = 0.04$ for the contribution of baryons, $H_0 = 72 \text{ km s}^{-1} \text{ Mpc}^{-1}$ for the present-day Hubble constant, $n_s = 0.96$ for the primordial spectral index and

$\sigma_8 = 0.8$ for the normalisation of the power spectrum. Within each Lagrangian region we increased the mass resolution and added the relevant high-frequency modes of the power spectrum, following the zoomed initial condition (ZIC) technique (Tormen et al. 1997). Outside these regions, particles of mass increasing with distance from the target halo are used, so as to keep a correct description of the large scale tidal field. Each high-resolution Lagrangian region is shaped in such a way that no low-resolution particle contaminates the central halo at $z = 0$ at least out to 5 virial radii². As a result, each region is sufficiently large to contain more than one interesting halo with no contaminants within its virial radius.

Initial conditions have been generated by adding a gas component only in the high-resolution region, by splitting each particle into two, one representing DM and another representing the gas component, with a mass ratio chosen to reproduce the cosmic baryon fraction. The mass of each DM particle is $m_{\text{DM}} = 8.47 \times 10^8 h^{-1} M_\odot$ and the initial mass of each gas particle is $m_{\text{gas}} = 1.53 \times 10^8 h^{-1} M_\odot$.

2.2 The simulation models

Simulations have been carried out with the TreePM-SPH GADGET-3 code, a more efficient version of the previous GADGET-2 code (Springel 2005). In the high-resolution region gravitational force is computed by adopting a Plummer-equivalent softening length of $\epsilon = 5 h^{-1} \text{ kpc}$ in physical units below $z = 2$, kept fixed in comoving units at higher redshift (see Borgani et al. 2006, for an analysis of the effect of softening on radiative simulations of galaxy clusters). As for the hydrodynamic forces, we assume the minimum value attainable by the SPH smoothing length of the B-spline kernel to be half of the corresponding value of the gravitational softening length. We carried out three different sets of simulations, that we tag as NR, CSF and AGN, whose description is provided here below.

- NR. Non-radiative hydrodynamical simulations, based on the entropy-conserving SPH (Springel and Hernquist 2002), with computation carried out using the B-spline kernel with adaptive smoothing constrained to attain a minimum value equal to half of the gravitational softening scale. The adopted artificial viscosity follows the scheme introduced by Monaghan (1997), with the inclusion of a viscosity limiter, as described by Balsara (1995) and Steinmetz (1996).

- CSF. Hydrodynamical simulations including the effect of cooling, star formation and SN feedback. Radiative cooling rates are computed by following the same procedure presented by Wiersma et al. (2009). We account for the presence of the cosmic microwave background (CMB) and of UV/X-ray background radiation from quasars and galaxies, as computed by Haardt and Madau (2001). The contributions to cooling from each one of eleven elements (H, He, C, N, O, Ne, Mg, Si, S, Ca, Fe) have been pre-computed using the publicly available CLOUDY photo-ionisation code (Ferland et al. 1998) for an optically thin gas in (photo-)ionisation equilibrium. Once metals are distributed from stars to surrounding gas particles, no process is included in the simulations to diffuse metals to neighbour gas particles. As a consequence, the metallicity field is quite noisy, since heavily enriched gas particles may have neighbour particles which are instead characterized by

² The virial radius, R_{vir} , is defined as the radius encompassing the overdensity of virialization, as predicted by the spherical collapse model (e.g., Eke et al. 1996).

low metallicity. This could in turn induce a noisy pattern in the computation of the cooling rates. In order to prevent such a spurious noise in the computation of radiative losses, we decided to smooth the metallicity field, for the only purpose of computing cooling rates, by using the same kernel used for the SPH computations (see also Wiersma et al. 2010).

This set of simulations includes star formation and the effect of galactic outflows triggered by SN explosions. As for the star formation model, gas particles above a threshold density of 0.1 cm^{-3} and below a temperature threshold of $2.5 \times 10^5 \text{ K}$ are treated as multiphase, so as to provide a sub-resolution description of the interstellar medium, according to the model originally described by Springel and Hernquist (2003). Within each multiphase gas particle, a cold and a hot-phase coexist in pressure equilibrium, with the cold phase providing the reservoir of star formation. The production of heavy elements is described by accounting for the contributions from SNe-II, SNe-Ia and low and intermediate mass stars, as described by Tornatore et al. (2007). Stars of different mass, distributed according to a Chabrier IMF (Chabrier 2003), release metals over the time-scale determined by the mass-dependent life-times of Padovani and Matteucci (1993). Kinetic feedback is implemented according to the model by Springel and Hernquist (2003): a multi-phase star particle is assigned a probability to be uploaded in galactic outflows, which is proportional to its star formation rate. We assume $v_w = 500 \text{ km s}^{-1}$ for the outflow velocity, while assuming a mass-upload rate that is two times the value of the star formation rate of a given particle.

- **AGN.** Radiative simulations including the same physical processes as in the CSF case, but also the effect of AGN feedback. Our model for the growth of SMBH and related AGN feedback is based on the original implementation presented by Springel et al. (2005) (see also Di Matteo et al. 2005) and quite similar to the one presented in Fabjan et al. (2010). Here below we briefly describe the BH feedback model used for our simulations, while we refer to the recently submitted paper by Ragone-Figueroa et al. (2013) for a more detailed description.

- *SMBH seeding and growth.* We represent SMBHs with collisionless particles, interacting only via gravitational forces. During the simulation, we periodically perform the identification of DM halos using an on-the-fly Friends-of-Friends (FoF) algorithm. When a DM halo is more massive than a given threshold M_{th} and does not already contain a SMBH, we seed it with a new BH with an initial small mass of $M_{seed} = 5 \times 10^6 h^{-1} M_\odot$. We set $M_{th} = 2.5 \times 10^{11} h^{-1} M_\odot$. The SMBH grows with an accretion rate given by the Bondi formula (Bondi 1952), and it is Eddington limited³. For each BH, the corresponding Bondi accretion rate is estimated using the local gas density assigned at the BH position by the same SPH spline kernel used for the hydrodynamic computations. The BH dynamical mass is updated according to the accretion rate, but we do not subtract the corresponding mass from the surrounding gaseous component. This results in a mass non-conservation of the order of at most a fraction of percent of the cluster central galaxy stellar mass, but improves the positioning of the SMBH particle and, more important, avoids the gas depletion in the BH surroundings, that, at the resolution of our simulations, would take place on exceedingly large scales.

- *SMBH advection.* As recently also discussed by Wurster and Thacker (2013) and Newton and Kay (2013), numerical effects can drift BHs, originally seeded in DM halos, outside such halos. In order to pin BHs at the centre of galaxies, at each time step we reposition the BH particles at the position of the neighbour particle, of any type (i.e. DM, gas or star), which has the minimum value of the gravitational potential. We perform the search of such a particle within the gravitational softening of the SMBH. When two BHs are within the gravitational softening and their relative velocity is smaller than 0.5 of the sound velocity of the surrounding gas, we merge them and we place the resulting BH at the position of the most massive one.

Note that we use the gravitational softening as a searching length, rather than the BH smoothing length as in most previous implementations, for both the advection and the merging algorithms. Given the gravitational nature of the numerical processes responsible for drifting the BHs away from galaxies, as well as the physical processes leading to BH merging, this length scale is the most appropriate to be used. In addition, at the resolution of our simulations, the BH smoothing length is unreasonably large for these purposes, and significantly larger than the gravitational softening. In particular, if we use the former for searching the minimum potential particle, BHs dwelling in satellite halos could often be spuriously displaced to the center of a more massive DM halo, and immediately would merge with the BH dwelling there. This numerical over-merging affects the mass function of BHs, thus spuriously increasing by merging the number of high-mass BHs, and correspondingly depleting the number of BHs at low and intermediate masses. We verified that numerical BH overmerging is significantly reduced by repositioning within the gravitational softening length.

- *Thermal Energy distribution.* In our model, the SMBH growth produces an energy determined by a parameter ϵ_r which gives the fraction of accreted mass which is converted in energy. Another parameter ϵ_f defines the fraction of extracted energy that is thermally coupled to the surrounding gas. In our implementation, both of these parameters, ϵ_r and ϵ_f , are given a value of 0.2. Finally, we assume a transition from a ‘quasar’ phase to a ‘radio’ mode of the BH feedback (see also Sijacki et al. 2007; Fabjan et al. 2010). This happens when the accretion rate becomes smaller than a given limit, $\dot{M}_{BH}/\dot{M}_{Edd} = 10^{-2}$. In this case, we increase the feedback efficiency ϵ_f by a factor of four. In the original implementation by Springel et al. (2005), the thermal energy from the BHs was simply added to the specific internal energy of gas particles. As a consequence, whenever this external energy was given to a star-forming gas particle, it was almost completely lost. This happens because in the effective model of star formation and feedback (Springel and Hernquist 2003), the internal energy of star-forming particles converges to the equilibrium energy of the inter-stellar medium on a very short time scale, and the equilibrium energy is independent on the specific internal energy of the gas (see discussion in Ragone-Figueroa et al. 2013). To avoid this, whenever a star-forming gas particle receives energy from a SMBH, we now calculate the temperature at which it would heat the cold gas phase⁴. If this temperature is larger than the average temperature of the gas particle (before receiving AGN energy), we consider

³ As explained in the Appendix of Ragone-Figueroa et al. (2013), the α -modified Bondi accretion rate employed in our model is characterized by an adimensional factor $\alpha = 100$.

⁴ The AGN energy is given to the hot and cold phase in proportion to their mass.

the particle not to be multi-phase anymore and prevent it from forming stars. The particle is, however, subject to normal radiative cooling. We also add a temperature threshold of 5×10^4 K as a further condition, besides density, for a gas particle to become multi-phase and form stars. This is needed because in our new scheme a dense gas particle can be very hot: if it became star-forming again, it would immediately lose all of its internal specific energy in excess to the equilibrium one.

2.3 Identification of clusters

The identification of clusters proceeds by running first a FoF algorithm in the high-resolution regions, which links DM particles using a linking length of 0.16 times the mean interparticle separation. The centre of each halo is then identified with the position of the DM particle, belonging to each FoF group, having the minimum value of the gravitational potential. Starting from this position, and for each considered redshift, a spherical overdensity algorithm is employed to find the radius R_Δ encompassing a mean density of Δ times the critical cosmic density at that redshift, $\rho_c(z)$. In the present work, we consider values of the overdensity⁵ $\Delta = 2500, 500$ and 180 . For the sake of completeness, we also consider the virial radius which defines a sphere enclosing the virial density $\Delta_{\text{vir}}(z)\rho_c(z)$, predicted by the spherical collapse model: $\Delta_{\text{vir}} \approx 93$ at $z = 0$ and ≈ 151 at $z = 1$ for the cosmological model assumed by our simulations (Bryan and Norman 1998).

In total, we end up with a sample of about 160 clusters and groups having $M_{\text{vir}} > 3 \times 10^{13} h^{-1} M_\odot$ at $z = 0$. This number is larger at higher redshift: ~ 240 systems at $z = 0.5$ and ~ 200 at $z = 1$. In Fig. 1 we show the cumulative number of clusters within the AGN set of simulations as a function of their mass M_{vir} at $z = 0, 0.5, 1$.

2.4 Computing the observable quantities

In order to analyse the results of our simulations, we will study several thermodynamical and chemodynamical properties which can be directly compared with observational data, and which have been widely studied by different simulations. Here we briefly describe how these quantities have been computed from our simulations.

- **X-ray luminosity.** This quantity is computed by summing the contributions to the emissivity, ϵ_i , carried by all the gas particles within the region R_Δ where L_X is computed:

$$L_X = \sum_i \epsilon_i = \sum_i n_{e,i} n_{H,i} \Lambda(T_i, Z_i) dV_i, \quad (1)$$

where $n_{e,i}$ and $n_{H,i}$ are the number densities of electrons and of hydrogen atoms, respectively, associated with the i -th gas element of given density ρ_i , temperature T_i , mass m_i , metallicity Z_i , and volume $dV_i = m_i/\rho_i$. Furthermore, $\Lambda(T, Z)$ is the temperature- and metallicity-dependent emissivity computed within a given energy band. The energy-dependent emissivity for each particle is calculated using the plasma emission model by Raymond and Smith (1977). The spectra are computed by binning the emissivity within energy intervals, so as to have an energy resolution $\Delta E = 0.01$. Luminosities within a given energy band are then computed by integrating this energy-dependent emissivity within the appropriate

⁵ The corresponding radii approximately relate to the virial radius as $(R_{2500}, R_{500}, R_{180}) \approx (0.2, 0.5, 0.7) R_{\text{vir}}$ (e.g., Ettori et al. 2006).

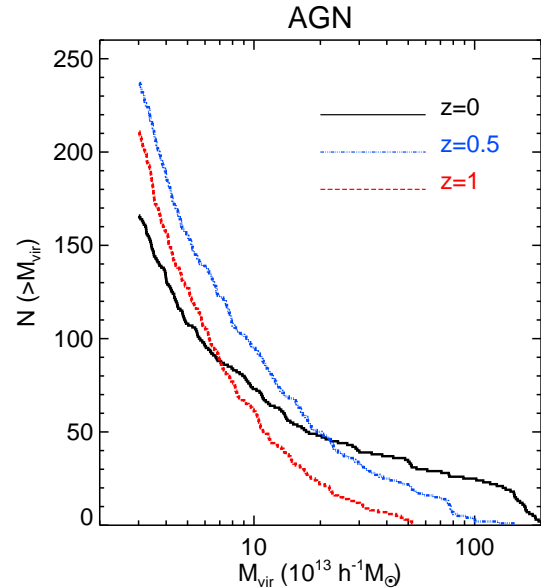


Figure 1. Cumulative distribution of masses M_{vir} for the set of clusters and groups identified in the AGN set of simulations. Solid black, dot-dashed blue and dashed red lines correspond to redshifts $z = 0, 0.5$ and 1 , respectively.

energy interval. We point out that the assumed cooling function adopted for the computation of X-ray luminosity depends on a global metallicity, rather than accounting for the contributions from all the chemical species followed in our simulations. In the following, we will present results on the X-ray luminosity as computed within the $[0.1 - 2.4]$ keV energy band.

- **Temperature.** Different proxies to the X-ray observational definition of temperature have been proposed in the literature. In general, the ICM temperature can be estimated as

$$T = \frac{\sum_i w_i T_i}{\sum_i w_i}, \quad (2)$$

where T_i is the temperature of the i -gas element, which contributes with the weight w_i . The mass-weighted definition of temperature, T_{mw} , is recovered for $w_i = m_i$, which also coincides with the electron temperature for a fully ionised plasma. The emission-weighted temperature would be instead recovered for $w_i = \epsilon_i$. On the contrary, the spectroscopic-like estimate of temperature, T_{sl} , is recovered from Eq. 2 by using the weight $w_i = \rho_i m_i T_i^{\alpha-3/2}$ with $\alpha = 0.75$ (Mazzotta et al. 2004). In the Bremsstrahlung regime ($T \gtrsim 2 - 3$ keV), this temperature estimator has been shown to provide a close match to the actual spectroscopic temperature, obtained by fitting X-ray spectra of simulated clusters with a single-temperature plasma model. When measuring the spectroscopic-like temperature T_{sl} of our systems, we follow the procedure described by Vikhlinin (2006), which generalizes the analytic formula originally introduced by Mazzotta et al. (2004) to include relatively cold clusters with temperature below 3 keV.

- **Entropy.** This is another useful quantity to characterise the thermodynamical status of the ICM (Voit 2005). We use the standard definition of entropy usually adopted in X-ray studies of galaxy clusters:

$$K_\Delta = k_B T_\Delta n_{e,\Delta}^{-2/3}, \quad (3)$$

where $n_{e,\Delta}$ is the electron number density computed at R_Δ , and k_B is the Boltzmann constant.

- Total thermal content. A useful proxy to the total thermal content of the ICM is the quantity $Y_X = M_g T$, with M_g being the gas mass and T one estimator of the global ICM temperature (e.g., Kravtsov et al. 2006). In our case, we will use two slightly different definitions of Y_X , the mass-weighted, $Y_{X,mw} = M_g T_{mw}$, and the spectroscopic-like, $Y_{X,sl} = M_g T_{sl}$, estimates. Being a proxy of the total thermal content of the ICM, Y_X turns out to be also a robust mass proxy, whose scaling relation against total cluster mass has a low scatter and is almost independent on the physical processes included in the simulations (Kravtsov et al. 2006; Stanek et al. 2010; Fabjan et al. 2011). In order to minimize the contribution to the scatter from the cluster central regions, Kravtsov et al. (2006) showed that the temperature should be estimated by excising the regions within $0.15R_{500}$. We will also adopt this procedure in the following.

- Pressure. By assuming an ideal gas equation of state, we compute the volume-weighted estimate of the gas pressure as

$$P = \frac{\sum_i p_i dV_i}{\sum_i dV_i}, \quad (4)$$

where $p_i = (k_B/\mu m_p)\rho_i T_i$ and dV_i are the contributions to pressure and volume, respectively, of each considered gas particle (μ and m_p being the mean atomic weight and the proton mass, respectively).

- Metallicity of the ICM. From an observational point of view, this quantity is computed through a spectral fitting procedure, by measuring the equivalent width of emission lines associated with a transition between two heavily ionised states of a given element. The simplest proxy to this spectroscopic measure of the ICM metallicity is, therefore, the emission-weighted definition,

$$Z_{ew} = \frac{\sum_i Z_i m_i \rho_i \Lambda(T_i, Z_i)}{\sum_i m_i \rho_i \Lambda(T_i)}, \quad (5)$$

where Z_i , m_i , ρ_i and T_i are the metallicity, mass, density and temperature of the i -gas element, with the sum being performed over all the gas particles lying within the cluster extraction region. Rasia et al. (2008) showed that the emission-weighted estimator of Eq. 5 provides values of metallicity that are quite close to the actual spectroscopic ones, at least for iron and silicon, while abundance of oxygen can be severely biased in high-temperature, $T \gtrsim 3$ keV, systems.

Since both simulated and observed metallicity radial profiles are characterised by significant negative gradients, we expect the “true” mass-weighted metallicity,

$$Z_{mw} = \frac{\sum_i Z_i m_i}{\sum_i m_i}, \quad (6)$$

to be lower than the “observed” emission-weighted estimate.

3 GENERAL X-RAY PROPERTIES

Before presenting the general X-ray properties of our sample of galaxy clusters, we highlight results from previous works that analyze different aspects of the same suite of simulations. Together, these results establish a reasonable level of consistency with observations with regards to the baryonic content of the clusters, emphasize the important role of radiative and feedback processes, and provide important calibrations for observational tests.

Generally speaking, as shown in Planelles et al. (2013), including the effect of AGN feedback helps to alleviate tension with observations for the stellar, the hot gas and the total baryon mass fractions. However, both of our radiative simulation sets predict a trend for the stellar mass fraction with cluster mass that is weaker than observed. On the other hand, this tension depends on the particular set of observational data considered. For massive clusters, the ratio between the cluster baryon content and the cosmic baryon fraction, Y_b , when computed at R_{500} , is nearly independent of the physical processes included and characterized by a negligible redshift evolution. At smaller radii, i.e. R_{2500} , the typical value of Y_b slightly decreases, by an amount that depends on the physics included in the simulations, while its scatter increases by a factor of two. These results have interesting implications for the cosmological applications of the baryon fraction in clusters.

Some of the tensions with observations may be due to difficulties in accounting for the diffuse stellar content, distinct from cluster member galaxies. Cui et al. (2013) have carried out a detailed analysis of the performance of two different methods to identify the diffuse stellar light. One of the methods separates the BCG from the ‘diffuse stellar component’ (DSC) via a dynamical analysis. The other is inspired by the standard observational technique: mock images are generated from simulations, and a standard surface brightness limit (SBL) is assumed to disentangle the BCG from the intra-cluster light (ICL). Significant differences are found between the ICL and DSC fractions computed with these two methods. The use of a brighter SBL can reconcile the ICL and DSC fractions but the exact value, as calibrated by the simulations, is quite sensitive to feedback.

Moreover, Ragono-Figueroa et al. (2013) investigated some problems that are common throughout the literature of numerical simulations of galaxy clusters that also include the effect of AGN feedback. For example, the inclusion of AGN feedback helps to reduce the stellar mass content of BCG galaxies, yet their stellar masses remain three times higher than observed. Correspondingly, there is still some tension between predictions and observations of the structural properties of BCGs, namely, larger half-light radii and indications of a flattening of the stellar density profiles on scales $\gtrsim 10$ kpc, much larger than observed. In addition, the BCGs stellar velocity dispersions are too large, but the implementation of the AGN feedback has little impact here.

3.1 Self-similar scaling relations

The simplest model to describe the properties of the ICM is the self-similar model originally derived by Kaiser (1986). This model assumes an Einstein–de Sitter background cosmology, that the shape of the power spectrum of fluctuations is strictly a power law and that no characteristic scales are introduced in the collapse process that leads to cluster formation. The first two assumptions amount to assume that no characteristic scale is present in the underlying cosmological model. The third assumption is naturally satisfied in the case that gravity is the only process driving halo collapse and gas heating. The self-similar model further assumes clusters to be spherically symmetric and in hydrostatic equilibrium (HE). A further key assumption of this model is that the logarithmic slopes of gas density and temperature profiles, which enter in the HE equation to provide the mass within a given radius, are independent of the cluster mass (see Kravtsov and Borgani 2012, for a recent review). In such self-similar model several simple relations between different X-ray properties of the gas in clusters can be predicted.

Here we provide some of the scaling relations that will be relevant for our analysis.

If, at redshift z , M_Δ is the mass contained within the radius R_Δ , enclosing a mean overdensity Δ times the critical cosmic density⁶, the total enclosed mass scales with temperature as:

$$M_\Delta \propto T_\Delta^{3/2} E^{-1}(z), \quad (7)$$

where T_Δ is the gas temperature measured at R_Δ . This relation between mass and temperature can be turned into scaling relations among other observable quantities.

Assuming that the gas distribution traces the dark matter distribution and that the thermal Bremsstrahlung process dominates the emission from the ICM plasma, the X-ray luminosity scales as

$$L_{X,\Delta} \propto M_\Delta \rho_c T_\Delta^{1/2} \propto T_\Delta^2 E(z). \quad (8)$$

Within the self-similar model, the entropy computed at a fixed overdensity Δ (see Eq. 3), scales with temperature and redshift according to

$$K_\Delta \propto T_\Delta E^{-4/3}(z). \quad (9)$$

As for Y_X , its self-similar scaling against mass computed within R_Δ is predicted to be

$$Y_{X,\Delta} \propto M_\Delta^{5/3} E^{2/3}(z). \quad (10)$$

A number of observations of representative samples of galaxy clusters in the local Universe have established that scaling relations predicted by the self-similar model do not match the observational results. For instance, the relation between X-ray luminosity and mass is steeper than the self-similar prediction (e.g., Chen et al. 2007). Consistently with the L_X - M relation, the observed L_X - T scaling is also steeper than predicted (e.g., Markevitch 1998; Arnaud and Evrard 1999; Osmond and Ponman 2004; Pratt et al. 2009), $L_X \propto T^\alpha$ with $\alpha \simeq 2.5 - 3$ for clusters ($T \gtrsim 2$ keV) and possibly even steeper for groups ($T \lesssim 1$ keV). Furthermore, the measured gas entropy in central regions is higher than expected (e.g., Sun et al. 2009; Pratt et al. 2010), especially for poor clusters and groups, with respect to the $K \propto T$ predicted scaling. This extra entropy prevents the gas from being compressed to high densities, reducing its X-ray emissivity compared to the self-similar prediction.

These discrepancies between the self-similar model and the observations have motivated the idea that, besides gravity, some important physics related with the baryonic component is missing in the model. The main non-gravitational physical processes thought to be responsible for boosting the entropy of the ICM are heating from astrophysical sources, such as SNe and AGN, and the removal of low-entropy gas via radiative cooling (e.g. Voit 2005). Lower-mass systems are affected more than massive objects, thus breaking the self-similarity of the scaling laws and providing, therefore, a probe of the star formation and feedback processes operating in cluster galaxies.

3.2 Scaling relations at $z = 0$

In this Section we analyse the scaling relations for our sample of simulated clusters and groups, paying special attention to the ef-

fect that the different physical models have on them. In particular, we analyse the $L_X - T$, $K - T$, $Y_X - M$ and $T - M$ relations at $z = 0$. Only clusters with $M_{vir} \gtrsim 3 \times 10^{13} h^{-1} M_\odot$ within our NR, CSF, and AGN simulation sets are included in our analysis. Unless otherwise stated, we compute these scaling relations adopting $\Delta = 500$ and, therefore, all quantities are evaluated within R_{500} . The reason for this choice is that, typically, R_{500} corresponds to the most external radius out to which detailed X-ray observations (e.g., Maughan 2007; Vikhlinin et al. 2009; Sun et al. 2009; Pratt et al. 2009), possibly in combination with SZ observations (e.g. Planck Collaboration et al. 2011), are provided.

We will use the T_{sl} estimator for the temperature in all the comparisons with X-ray data. However, it is well known that, compared with the mass-weighted temperature, the T_{sl} produces larger scatter in the scaling relations (e.g., Fabjan et al. 2011), owing to its sensitivity to the contribution of the cold component of the gas temperature distribution. In order to analyze the intrinsic scatter in these relations and their behaviour as mass proxies, we will compute them by using both estimates of the ICM temperature, that is, T_{sl} and T_{mw} . Correspondingly, we will show the $Y_X - M$ relation for both estimates of Y_X ($Y_{X,sl}$ and $Y_{X,mw}$). In addition, in order to reduce the scatter in the scaling relations involving temperature (e.g., Pratt et al. 2009, and references therein) and to better reproduce the procedure of observational analyses, we exclude the central regions, $r < 0.15 R_{500}$, in the computation of the temperature.

For each set of cluster properties, $(X, F) = (T, L_X)$, (T, K) , (M, Y_X) and (M, T) , we fit to our sample of simulated clusters at $z = 0$ a power-law scaling relation of the form

$$F = C_0 \left(\frac{X}{X_0} \right)^\alpha, \quad (11)$$

by minimising the unweighted χ^2 in log space. Here $X_0 = 6$ keV if $X = T$ and $X_0 = 5.0 \times 10^{14} h^{-1} M_\odot$ if $X = M$. The best-fitting parameters α and C_0 for each relation are summarised in Table 1. Following a similar approach to that presented in Short et al. (2010), the scatter in these relations, $\sigma_{\log_{10} F}$, is estimated as the rms deviation of $\log_{10} F$ from the mean relation:

$$\sigma_{\log_{10} F}^2 = \frac{1}{N-2} \sum_{i=1}^N \left[\log_{10} F_i - \alpha \log_{10} \left(\frac{X}{X_0} \right) - \log_{10} C_0 \right]^2, \quad (12)$$

where N is the number of individual data points. The scatter about each relation is also listed in Table 1.

In order to compare with observational data, we use a selection of representative observational samples, mainly from Pratt et al. (2009), Pratt et al. (2010), Sun et al. (2009), Mahdavi et al. (2013) and Eckmiller et al. (2011). To ‘scale’ these observational data to $z = 0$ for comparison with our simulated clusters, the correction factor $E(z)^n$ is included, thus removing the self-similar evolution predicted by Eqs. (8)–(10).

Before presenting the results of our analysis, we briefly describe the main characteristics of each of the observational data sets we compare with. Pratt et al. (2009) and Pratt et al. (2010) examine the X-ray properties of 31 nearby galaxy clusters from the Representative *XMM-Newton* Cluster Structure Survey (REXCESS, Böhringer et al. 2007). This sample, which includes clusters with temperatures in the range 2–9 keV, has been selected in X-ray luminosity only, with no bias towards any particular morphological type. According to their central densities, clusters in this sample have been classified as relaxed, cool-core (CC) systems or as morphologically disturbed or non-cool core (NCC) systems. These data are particularly suitable for a comparison with our simulated cluster

⁶ $M_\Delta = \Delta \rho_c(z) (4\pi/3) R_\Delta^3$, where $\rho_c(z) = 3H_0^2 E(z)^2 / 8\pi G$ is the critical density and $E(z) \equiv H(z)/H_0 = [(1+z)^3 \Omega_m + \Omega_\Lambda]^{1/2}$ in a spatially-flat Λ CDM cosmological model.

Table 1. Best-fit parameters (with 1σ errors) for the X-ray scaling relations for our sample of clusters in the NR, CSF and AGN sets at $z = 0$. Only clusters with $M_{vir} \gtrsim 3 \times 10^{13} h^{-1} M_{\odot}$ have been considered. All quantities have been computed within R_{500} . For each set of cluster properties, a power-law scaling relation given by Eq. 11 is fit to our sample of simulated clusters. According to this fitting, C_0 , α and $\sigma_{\log_{10} F}$ (see Eq. 12) represent the normalisation, the slope and the scatter of the different relations, respectively. The normalisation C_0 has units of $10^{44} \text{erg s}^{-1}$, keV cm^2 , $10^{14} h^{-1} M_{\odot} \text{keV}$, and keV for $L_X - T$, $K - T$, $Y_X - M$, and $T - M$, respectively.

Relation	C_0	α	$\sigma_{\log_{10} F}$
NR simulation			
$T_{\text{sl}}-M$	3.24 ± 0.07	0.51 ± 0.01	0.07
$T_{\text{mw}}-M$	4.89 ± 0.06	0.65 ± 0.01	0.03
$Y_{X,\text{sl}}-M$	2.34 ± 0.06	1.53 ± 0.01	0.09
$Y_{X,\text{mw}}-M$	3.53 ± 0.06	1.67 ± 0.01	0.05
$L_{X,[0.1-2.4] \text{ keV}}-T_{\text{sl}}$	61.08 ± 4.53	2.29 ± 0.04	0.16
$L_{X,[0.1-2.4] \text{ keV}}-T_{\text{mw}}$	23.16 ± 1.25	1.85 ± 0.03	0.15
$K-T_{\text{sl}}$	2588.30 ± 99.21	1.17 ± 0.02	0.08
$K-T_{\text{mw}}$	1550.44 ± 52.64	0.93 ± 0.02	0.09
CSF simulation			
$T_{\text{sl}}-M$	4.80 ± 0.08	0.55 ± 0.01	0.05
$T_{\text{mw}}-M$	5.40 ± 0.08	0.60 ± 0.01	0.05
$Y_{X,\text{sl}}-M$	2.55 ± 0.06	1.66 ± 0.01	0.08
$Y_{X,\text{mw}}-M$	2.87 ± 0.06	1.71 ± 0.01	0.07
$L_{X,[0.1-2.4] \text{ keV}}-T_{\text{sl}}$	7.49 ± 0.61	2.17 ± 0.05	0.22
$L_{X,[0.1-2.4] \text{ keV}}-T_{\text{mw}}$	5.80 ± 0.43	2.00 ± 0.05	0.21
$K-T_{\text{sl}}$	2027.88 ± 42.16	1.02 ± 0.01	0.06
$K-T_{\text{mw}}$	1787.95 ± 37.55	0.94 ± 0.01	0.06
AGN simulation			
$T_{\text{sl}}-M$	5.02 ± 0.07	0.54 ± 0.01	0.04
$T_{\text{mw}}-M$	5.23 ± 0.07	0.55 ± 0.01	0.04
$Y_{X,\text{sl}}-M$	3.19 ± 0.08	1.73 ± 0.01	0.08
$Y_{X,\text{mw}}-M$	3.32 ± 0.08	1.74 ± 0.01	0.07
$L_{X,[0.1-2.4] \text{ keV}}-T_{\text{sl}}$	9.48 ± 0.77	2.46 ± 0.05	0.23
$L_{X,[0.1-2.4] \text{ keV}}-T_{\text{mw}}$	8.56 ± 0.67	2.43 ± 0.05	0.22
$K-T_{\text{sl}}$	1686.51 ± 33.27	0.94 ± 0.01	0.05
$K-T_{\text{mw}}$	1619.83 ± 31.76	0.93 ± 0.01	0.06

samples because spectral temperatures, luminosities, masses and entropies are tabulated within R_{500} .

Sun et al. (2009) present an analysis of 43 nearby galaxy groups ($kT_{500} = 0.7 - 2.7 \text{ keV}$ or $M_{500} = 10^{13} - 10^{14} h^{-1} M_{\odot}$, $0.012 < z < 0.12$), based on *Chandra* archival data. They trace gas properties out to at least R_{2500} for all 43 groups. For 11 groups, gas properties are robustly derived to R_{500} and, for an additional 12 groups, they derive properties at R_{500} from extrapolation.

In a recent work within the Canadian Cluster Comparison Project (CCCP), Mahdavi et al. (2013) present a study of multi-wavelength X-ray and weak lensing scaling relations for a sample of 50 clusters of galaxies in the redshift range $0.15 < z < 0.55$. After considering a number of scaling relations, they found that gas mass is the most robust estimator of weak lensing mass, yielding 15 ± 6 per cent intrinsic scatter at r_{500}^{WL} , whereas the pseudo-pressure Y_X yields a consistent scatter of 22 ± 5 per cent.

In order to test local scaling relations for the low-mass range, Eckmiller et al. (2011) compiled a statistically complete sample of 112 galaxy groups from the X-ray selected *HIFLUGCS*, *NORAS*, and *REFLEX* catalogues (Reiprich and Böhringer 2002; Böhringer et al. 2000, 2004, respectively). Groups were selected by

applying an upper limit to the X-ray luminosity, which was determined homogeneously for all three parent catalogues, plus a lower redshift cut to exclude objects that were too close to be observed out to sufficiently large radii. In this work, only a subsample of 26 local groups (median redshift 0.025), observed with the *Chandra* telescope with sufficient exposure time ($\gtrsim 10 \text{ ks}$), was investigated. Temperature, metallicity, and surface brightness profiles were created for these 26 groups, and used to determine the main physical quantities and scaling relations.

3.2.1 Mass scaling relations

Figure 2 shows the $T_{\text{mw}}-M$ and $T_{\text{sl}}-M$ relations (left and right panels, respectively) within R_{500} for the sample of clusters in our NR, CSF, and AGN runs. Results on the $T_{\text{mw}}-M$ relation are compared with the self-similar prediction, while results on the $T_{\text{sl}}-M$ relation are compared with observational data from Pratt et al. (2009) and Sun et al. (2009).

In agreement with previous analyses (e.g., Stanek et al. 2010; Fabjan et al. 2011), the $T_{\text{mw}}-M$ relation in the NR case has a slope in close agreement with the self-similar scaling, $\alpha \sim 0.65 \pm 0.01$, also with a tight scatter (see Table 1). In addition, whereas at the scale of high-mass systems this relation is relatively insensitive to baryon physics, at the scale of groups, $M_{500} \lesssim 10^{14} h^{-1} M_{\odot}$, a significant deviation from the self-similar expectation is present in the radiative simulations. The deviation is more significant for the AGN simulations due to the heating from the BH energy feedback, which is relatively more efficient in low-mass groups.

As for the comparison with observational data, we consider the mass–temperature relation using the spectroscopic-like estimator of temperature. As a word of caution in performing this comparison, we remind that we use here true cluster masses for simulations, while masses for the observational data shown in the right panel of Fig. 2 are based on X-ray data and the application of hydrostatic equilibrium. While it is beyond the scope of this paper to carry out a detailed analysis of biases in X-ray mass estimates, the evidence from simulation analyses indicates that X-ray masses may be underestimated by ~ 20 per cent (e.g., Nagai et al. 2007b; Rasia et al. 2012, and references therein).

We note that in the $T_{\text{sl}}-M$ relation, for a given mass, clusters in the NR runs are much cooler than observed, by an amount that is definitely larger than in the $T_{\text{mw}}-M$ relation. In addition, the scatter around the mean relation is larger than in the radiative runs. By definition (see Section 2.4) the spectroscopic-like temperature tends to give more weight to the relatively colder component of the gas temperature distribution (see also Mazzotta et al. 2004). In order to show the different degree of thermal complexity of the ICM generated by the different models, we show in Fig. 3 the temperature maps of a massive cluster for the NR, CSF and AGN cases. Quite apparently, in the NR simulations there is more gas in relatively small cold clumps that bias T_{sl} low and contribute to the increase in scatter⁷. A smaller amount of cold gas is instead present in the radiative simulations. For the CSF simulations, this is mostly due to gas removal by overcooling. As a result, only relatively hot gas, having longer cooling time, is present in substructures. In this case, a smaller amount of cold gas characterises not only the sub-clumps, but also the ram–pressure stripped gas that forms the comet-like features associated with merging events. As

⁷ We note that the coldest gas particles, those with temperature below 0.3 keV , are not taken into account in the computation of T_{sl} .

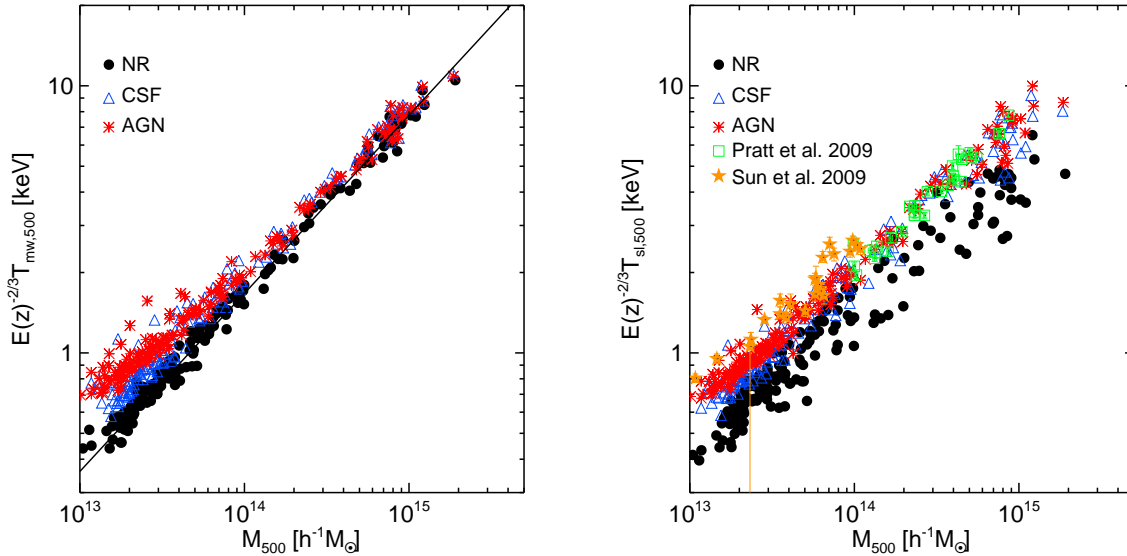


Figure 2. Mass-weighted (left panel) and spectroscopic-like (right panel) temperature as a function of total mass within R_{500} at $z = 0$. Results for our sample of clusters within the NR, CSF, and AGN runs as represented by black circles, blue triangles and red stars, respectively. On the left panel, our results are compared with the self-similar scaling (black continuous line). On the right panel, observational samples from Pratt et al. (2009) and Sun et al. (2009) are used for comparison.

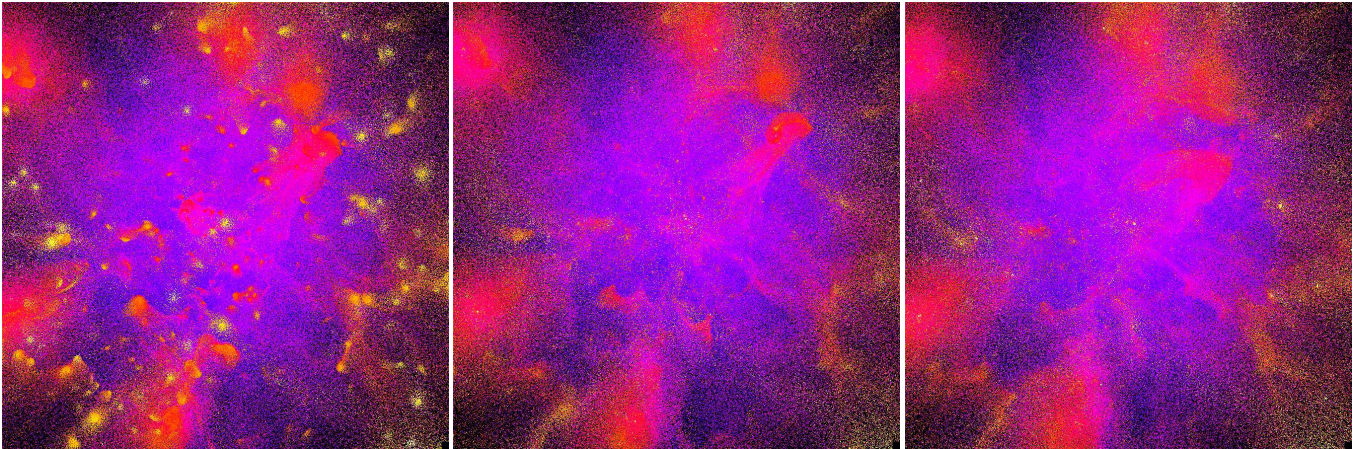


Figure 3. Temperature maps centered on a massive cluster having $M_{200} \simeq 1.3 \times 10^{15} h^{-1} M_{\odot}$. From left to right, panels show maps for the NR, CSF and AGN simulations. Each panel encompasses a physical scale of $6.25 h^{-1} \text{Mpc}$ a side. Colder regions are shown with brighter colours.

for the AGN simulation, in this case relatively cold gas is removed from sub-clumps by a twofold effect of BH feedback. Firstly, this feedback heats gas before a substructure is merged into the main cluster halo. Secondly, the more diffuse gas distribution makes sub-halos more prone to be ram-pressure stripped as they move through the hot pressurised atmosphere of the cluster. The smoother temperature distribution in the radiative simulations increases T_{sl} at fixed mass, with respect to the non-radiative case, and decreases the scatter due to the presence of cold clumps, thus bringing the simulated mass–temperature relation in better agreement with observations. Quite interestingly, the effect of AGN feedback in halos below $10^{14} h^{-1} M_{\odot}$ is that of slightly increasing T_{sl} with respect to the CSF simulations, thus producing a shallower slope of this scaling relation, in better agreement with observations. Despite the different manner in which cooling/heating processes remove gas

from subclumps in each case, the T_{sl} - M relations obtained in both of our radiative runs have similar normalisations and slopes. The fact that the slope we obtain for this relation is pretty similar in all cases ($\alpha \sim 0.5$) indicates that the T_{sl} - M relation is weakly sensitive to baryonic physics (e.g., Short et al. 2010). However, we see that none of our simulations reproduce the self-similar scaling for the T_{sl} - M relation.

As for the Y_X - M relation, we remind that both simulations (e.g., Kravtsov et al. 2006; Stanek et al. 2010; Short et al. 2010; Fabjan et al. 2011) and observations (e.g., Arnaud et al. 2007; Maughan 2007; Vikhlinin et al. 2009) indicate that Y_X is a low-scatter mass proxy, even in the presence of significant dynamical activity. Furthermore, X-ray observations have shown that the measured slope for this relation agrees with the self-similar prediction $\alpha = 5/3$ (see Eq. 10).

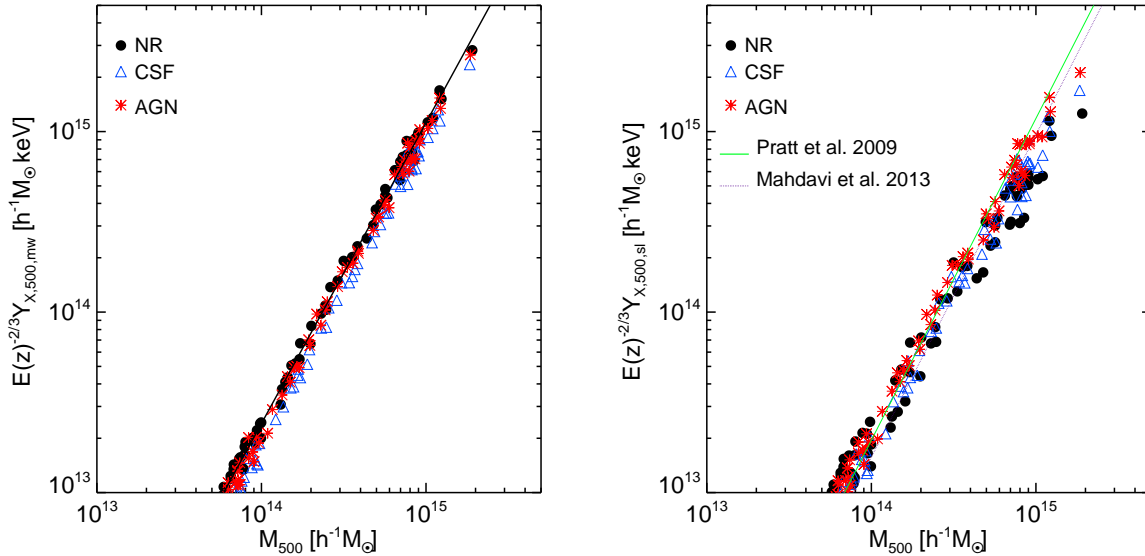


Figure 4. Relation between Y_X and total mass within R_{500} at $z = 0$. In the left panel, our results on the $Y_{X,mw}-M$ relation are compared with the self-similar scaling (black continuous line). In the right panel we compare our results on the $Y_{X,sl}-M$ relation with the observational results from Pratt et al. (2009) and Mahdavi et al. (2013). In both panels, results for our sample of clusters within the NR, CSF, and AGN runs as represented by black circles, blue triangles and red stars, respectively.

Figure 4 shows the local Y_X-M relation obtained for our sample of clusters within the NR, CSF, and AGN simulations. In the left panel, we show our results on the $Y_{X,mw}-M$ relation and compare it with the self-similar scaling. Based on this plot, we confirm that the total thermal content of the ICM is tightly connected to cluster mass in a way that is weakly sensitive to the inclusion of different physical processes affecting the evolution of the intra-cluster plasma (e.g. Kravtsov et al. 2006; Short et al. 2010; Fabjan et al. 2011; Kay et al. 2012, and references therein). Residual variations for the CSF simulations with respect to the NR ones are due to the removal of gas from the hot phase as a consequence of overcooling, which causes a decrease of Y_X at fixed mass. The mass-dependent efficiency of cooling in this case causes a small deviation from the self-similar slope of the NR simulations. Conversely, including AGN feedback has the effect of partially preventing gas removal from cooling, thus slightly increasing the normalisation of the $Y_{X,mw}-M$ relation.

$Y_{X,mw}$ is a key physical quantity since it is the X-ray analogue of the integrated Compton parameter y , a measure of the gas pressure integrated along the line-of-sight (e.g., Kravtsov et al. 2006). The total SZ signal, integrated over the cluster extent, is proportional to the integrated Compton parameter Y_{SZ} , which relates to Y_X as $Y_{SZ} D_A \propto Y_X$, where D_A is the angular distance to the system. Therefore, understanding the scaling and evolution of $Y_{X,mw}$ is important not only as a probe of the ICM physics, but also to exploit the combination of X-ray and SZ data (e.g., Arnaud et al. 2010).

In the right panel of Fig. 4, our results for the $Y_{X,sl}-M$ relation are compared with the observational relation from Pratt et al. (2009) and from Mahdavi et al. (2013). We remind the reader here that Pratt et al. (2009) estimated masses from the application of hydrostatic equilibrium to X-ray data, while Mahdavi et al. (2013) measured cluster masses from weak lensing data. The $Y_{X,sl}-M$ relation obtained from the NR simulations is shallower than the observed relations. The increase of T_{sl} when passing from the NR to

the CSF and the AGN sets also causes a corresponding progressive increase of Y_X , thus improving the agreement with observational results.

The fact that the CSF and AGN runs yield Y_X-M relations that are close to each other and also close to the self-similar prediction implies that Y_X must be relatively unaffected by the non-gravitational heating in these models. In the case of the AGN run, this arises because AGN feedback removes gas from the central regions of halos, reducing the gas mass within R_{500} , but this is offset by an increase in gas temperature caused by the continuous injection of energy from the BH feedback.

3.2.2 $L_X - T$ relation

Figure 5 shows the L_X-T_{sl} relation for the sample of clusters in our NR, CSF, and AGN sets. Here X-ray luminosities are computed in the [0.1–2.4] keV energy band. We compare with observational data on the scale of galaxy clusters and groups from Pratt et al. (2009) and Eckmiller et al. (2011), respectively. In this case there is no special reason to compare our results to predictions of the self-similar model. In fact, violation of self-similarity is expected as a consequence of computing L_X in a specific energy band and using T_{sl} instead of T_{mw} .

We note that the NR runs fail to reproduce the observed $L_X - T_{sl}$ relation and produce clusters that are more luminous than the observed ones. On the contrary, both of our radiative runs produce a significant reduction of X-ray luminosity at all scales obtaining, therefore, results that are closer to the observational data. In the CSF simulations the reduction of X-ray luminosity is the consequence of overcooling, which causes an exceedingly high removal of hot gas from the X-ray emitting phase and forces a too large fraction of gas to be converted into stars (e.g., Kravtsov et al. 2005; Fabjan et al. 2010; Puchwein et al. 2010; Sembolini et al. 2012; Planelles et al. 2013, and references therein). Quite interestingly, both the CSF and AGN models yield almost identical

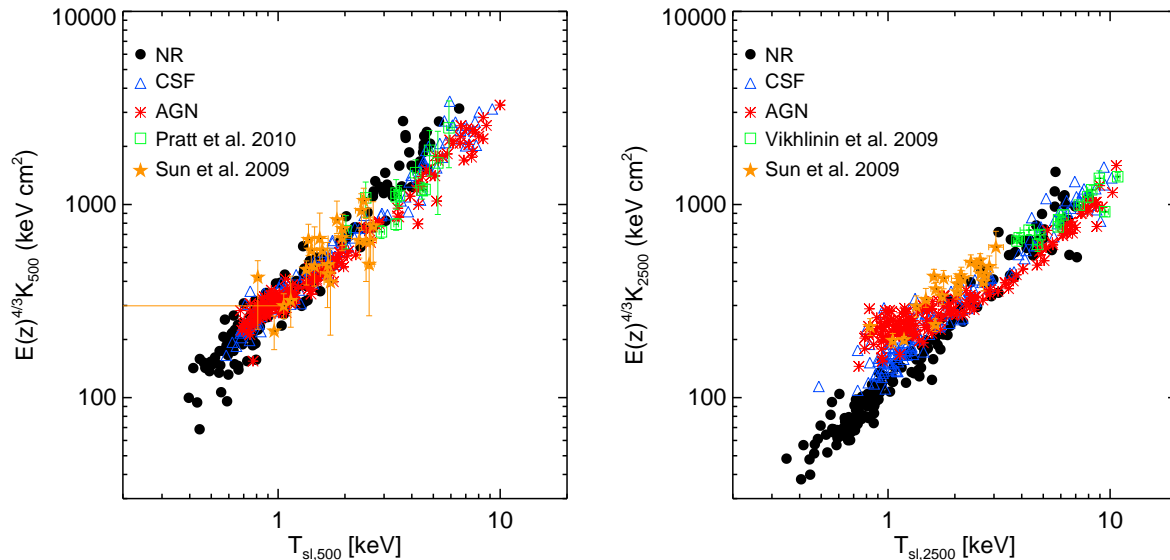


Figure 6. Entropy as a function of spectroscopic-like temperature at R_{500} (left panel) and at R_{2500} (right panel) at $z = 0$. Results for our simulated clusters within the NR, CSF, and AGN sets are shown as black circles, blue triangles and red stars, respectively. Observational results from Pratt et al. (2010), Sun et al. (2009) and Vikhlinin et al. (2009) are used for comparison.

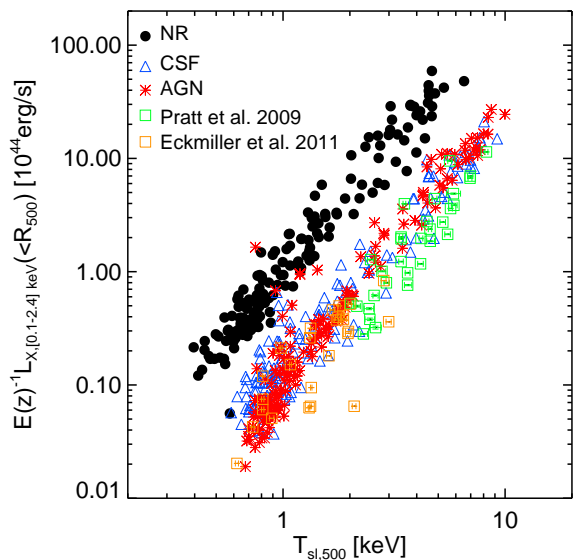


Figure 5. X-ray luminosity, computed within the $[0.1 - 2.4]$ keV energy band, as a function of spectroscopic-like temperature within R_{500} (excluding the central regions, $r < 0.15R_{500}$) at $z = 0$. Results for our sample of clusters within the NR, CSF, and AGN runs are represented by black circles, blue triangles and red stars, respectively. Observational results from Pratt et al. (2009) and Eckmiller et al. (2011) are used for comparison.

$L_{X,[0.1-2.4] \text{ keV}} - T_{sl}$ relations, despite the fact that the latter reduces the amount of stars to levels consistent with observational results (see Fig. 2 from Planelles et al. 2013; see also Puchwein et al. 2010; Battaglia et al. 2012b). In this case, gas removal by the action of AGN feedback compensates the larger amount of gas left in the diffuse phase by the reduction of star formation. Furthermore, AGN feedback is slightly more efficient in decreasing X-ray lumi-

nosity at the scale of galaxy groups, as a consequence of the more efficient removal of gas in less massive systems, with shallower potential wells. This turns into a steepening of the $L_X - T_{sl}$ relation with respect to the CSF case, thereby recovering the observational results better.

If we use instead the values of T_{sl} computed without excising the core regions, we would obtain similar $L_X - T_{sl}$ relations, in terms of normalisation and slope, for the three set of simulations. However, some low-mass systems show important deviations in their temperatures, contributing to increase the scatter around the mean relation, especially within the AGN simulations.

Our results are in line with previous results from simulations including different implementations of AGN feedback (e.g., Puchwein et al. 2008; Short et al. 2010; Fabjan et al. 2010). It is important to note that the AGN feedback implemented in these works differs among each other both in the implementation of the AGN feedback mechanism and in the treatment of the metallicity dependence of the cooling function. However, in all cases, results highlight the fact that, almost independently of the details of the heating mechanism, feedback energy associated with accretion onto SMBH is indeed able to reproduce a realistic $L_X - T$ relation.

3.2.3 $K - T$ relation

We show in Fig. 6 the relation between the entropy and the spectroscopic-like temperature at R_{500} (left panel) and R_{2500} (right panel) for our sample of simulated clusters in the NR, CSF, and AGN sets. We compare our results with observational data for clusters and groups from Pratt et al. (2010), Sun et al. (2009) and Vikhlinin et al. (2009).

At R_{500} we note that all simulation sets produce an entropy-temperature relation which is in good agreement with observational results at the group scale, with radiative simulations being more consistent with observations of massive clusters. However, this similarity of the scaling relation does not imply that different feedback mechanisms leave entropy unaffected at R_{500} within

groups. In fact, as discussed above, the value of T_{sl} at fixed mass increases for the radiative simulations, an effect which is more pronounced for the AGN case. As we shall discuss in Section 3.3.2, the increase of entropy in the CSF case is due to the combination of two effects: selective removal by cooling of low-entropy gas, which has shorter cooling time; and inflow of higher entropy gas from outer cluster regions caused by the lack of pressure support associated with overcooling. As in the AGN case, the increase of entropy in groups is instead due to gas heating that in fact prevents the excess of cooling. The corresponding increase of entropy in radiative simulations of groups causes a shift of all the points along the same direction traced by the K - T relation of the non-radiative runs. In massive systems, different feedback mechanisms have a small impact on the entropy level at R_{500} , so that the effect on the K - T relation is only induced by the variation of T_{sl} produced by the presence of cooling and of different feedback mechanisms.

As expected, the effects of the different ICM physics are more pronounced at R_{2500} (right panel of Fig. 6). At the scale of small clusters and groups, AGN feedback provides a significant increase of the entropy level, which causes a significant deviation with respect to the prediction of non-radiative simulations and better reproduces observational results on the entropy excess for systems with $T_{sl} \simeq 1$ keV.

3.3 Profiles of ICM properties

Radial profiles of the ICM thermal properties are more sensitive than scaling relations to the precise manner in which cooling, star formation and feedback processes are described in numerical simulations. In this Section we examine whether our different feedback schemes are able to reproduce the temperature, entropy and pressure profiles of observed local clusters.

Owing to the reference observational results that we will consider, in the following we will restrict the analysis of these radial profiles only to relatively massive clusters in our simulation sets, with $T_{sl,500} \gtrsim 3$ keV. Within our simulations we identify about 36 such objects at $z = 0$.

In order to examine the effect of the dynamical state of the clusters on the radial profiles, we divide our sample into dynamically relaxed and unrelaxed systems. We perform this classification by simply measuring the offset between the position of the potential minimum of the cluster and the centre of mass of all the particles within its virial radius (e.g., Crone et al. 1996; Thomas et al. 1998; Power et al. 2012). If this offset is larger (smaller) than 0.07 (in units of the cluster virial radius), then the cluster is considered to be dynamically unrelaxed (relaxed). With this classification, the fraction of relaxed systems found in our sample is ~ 80 per cent of the whole sample within each set of simulations.

3.3.1 Temperature profiles

The left panel of Fig. 7 shows the average spectroscopic-like temperature profile of clusters for our NR, CSF and AGN simulations out to R_{180} . All profiles have been normalised to the characteristic mean cluster temperature within R_{180} , $T_{sl,180}$. The mean temperature profile obtained from Leccardi and Molendi (2008b) is shown for comparison as a green region. Leccardi and Molendi (2008b) measured radial temperature profiles for a sample of ≈ 50 hot galaxy clusters, selected from the *XMM-Newton* archive. Most of the clusters in this sample ($\approx 2/3$) belong to the REFLEX Cluster

Survey catalog (Böhringer et al. 2004), a statistically complete X-ray flux-limited sample of 447 galaxy clusters, and a dozen objects belong to the *XMM-Newton* Legacy Project sample (Pratt et al. 2007), which is representative of an X-ray flux-limited sample with $z < 0.2$ and $kT > 2$ keV. Similarly to other X-ray measurements of temperature profiles (e.g., Sanderson et al. 2006; Vikhlinin et al. 2006; Pratt et al. 2007; Arnaud et al. 2010), the temperature peaks at $r \lesssim 0.2 R_{180}$, with a gentle decline at small radii, which is the signature for the presence of cool cores.

As already demonstrated by previous analysis of cluster simulations (e.g., Loken et al. 2002; Borgani et al. 2004; Kay et al. 2007; Pratt et al. 2007; Nagai et al. 2007a; Fabjan et al. 2010; Short et al. 2010; Vazza et al. 2010), almost independently of the physical processes included, the temperature profiles for our sample of galaxy clusters have a slope that agrees quite well with observations in outer cluster regions, $r \gtrsim 0.2 R_{180}$, where the effect of cooling and feedback is relatively unimportant. However, at such radii we note that the temperature profile for the NR simulations is systematically lower than for the radiative cases, and with a rather irregular behaviour. As already discussed in Section 3.2.1, this is a consequence of the spectroscopic-like estimate of the temperature, which gives more weight to the colder gas component associated with substructures, which are more prominent at relatively large radii (see also Fig. 3). Therefore, the wiggles in the NR profile are just due to the effects of substructures, that persist even after averaging over the set of simulated clusters.

As for the core regions, we see that in all cases simulated temperature profiles are higher than the observed ones. This discrepancy persists also in the presence of radiative cooling. As discussed above, this is a paradoxical effect of cooling due to the adiabatic compression of gas flowing in from cluster outskirts to compensate for the lack of pressure support caused by too much gas cooling out of the hot phase. To prevent this overcooling and reduce the central values of the temperature, one should require that a suitable feedback mechanism keeps the gas at an intermediate temperature. Since this “cool” gas formally has a short cooling time, preventing it from cooling out of the X-ray emitting phase requires heating from energy feedback to exactly balance radiative losses. The comparison of our results with observational data in the right panel of Fig. 7 shows that even AGN feedback is not effective in creating the correct structure of “cool cores” in massive galaxy clusters.

To look for differences between clusters in different dynamical states, the right panel of Fig. 7 shows the mean temperature profiles computed separately for the relaxed and unrelaxed cluster subsamples in our AGN set. Now we compare our results with the observed samples of cool core (CC) and non-cool core (NCC) clusters from Leccardi and Molendi (2008b). These authors classified clusters as CC if the central temperature is significantly lower than T_{180} , while morphologically disturbed or NCC systems are those for which the temperature profile does not significantly decrease. Admittedly, this classification is based on a criterion that is different from that we followed to classify clusters as relaxed and unrelaxed. Still, it is quite interesting to note that temperature profiles of our simulated clusters do not depend on their dynamical state. Our results extend to the AGN feedback case a similar result found by Eckert et al. (2013) for the non-radiative AMR simulations by Vazza et al. (2010). In general, profiles from simulations tend to agree better with results from NCC systems, which also display rather steep temperature gradients down to small radii. This result is consistent with the expectation that the adopted model of AGN feedback is not capable of producing the heating/cooling balance,

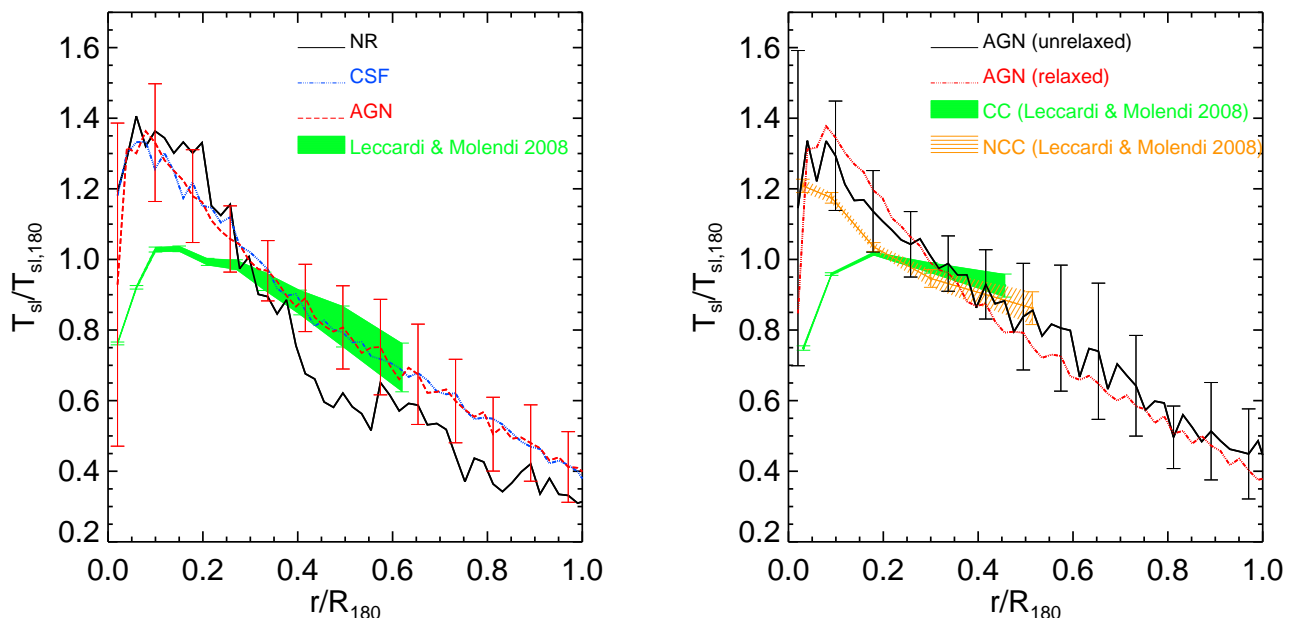


Figure 7. *Left panel:* mean $T_{sl}/T_{sl,180}$ radial profiles out to R_{180} at $z = 0$ for our sample of massive clusters with $T_{sl,500} > 3$ keV. Black continuous, blue dotted-dashed and red dashed lines stand for the mean profiles in the NR, CSF and AGN simulations. For the sake of clarity, error bars showing 1σ scatter are shown only for the AGN case. *Right panel:* mean $T_{sl}/T_{sl,180}$ radial profiles computed separately for the relaxed/unrelaxed cluster subsamples in our AGN run. Black continuous and red dotted-dashed lines stand for the mean profiles of unrelaxed and relaxed systems, respectively, with the 1σ scatter only shown for the unrelaxed systems. In both panels, we compare our results with the observed temperature profiles from Leccardi and Molendi (2008b), which are represented by the coloured shadowy areas.

which is responsible for the stabilisation of cool cores in relaxed systems.

Our results, which are generally in line with independent analyses of simulations including different versions of AGN thermal feedback, are not able to convincingly reproduce the observed thermal properties of cluster core regions (e.g., Kravtsov and Borgani 2012). The reason for these discrepancies may be related to both the limited numerical resolution achievable with cosmological simulations, and the difficulty of providing a coherent description of the complex interplay between AGN feedback and a number of other physical processes (e.g., turbulence ICM motions, non-thermal pressure support, magnetic fields).

In addition, observational results indicate that sub-relativistic jets from the BH hosted in central cluster galaxies shocks the surrounding ICM, thereby producing bubbles of high-entropy gas. In this regard, recent numerical experiments (e.g. Omma et al. 2004; Gaspari et al. 2011; Barai et al. 2013) indicate that the inclusion of mechanical AGN feedback in cosmological simulations seems to be an improvement to be implemented (e.g. Martizzi et al. 2012), along with the exploration of accretion models different from the standard Bondi criterion.

3.3.2 Entropy profiles

The entropy distribution of the ICM has long been a crucial diagnostic to study the impact of non-gravitational processes, related to galaxy formation, on the diffuse cosmic baryons. In fact, entropy preserves a record of the physical processes that determine the thermal history of the ICM (e.g., Voit 2005, for a review).

Analytical models based on spherical collapse predict that,

if shock heating is the only mechanism acting to raise the entropy of the gas, entropy scales with radius as $K \propto r^{1.1}$ outside of central cluster regions (e.g., Tozzi and Norman 2001). Cosmological simulations that only include gravitational heating confirm this prediction although give rise to slightly steeper entropy profiles in cluster outskirts, with $K \propto r^{1.2}$ (e.g., Voit et al. 2005; Nagai et al. 2007a; Planelles and Quilis 2009). These results from simulations are generally in line with observational results (e.g. Pratt et al. 2010; Eckert et al. 2013).

At small radii, observed entropy profiles display a variety of behaviours, depending on their dynamical state. Indeed relaxed CC systems show steadily decreasing profiles down to the smallest sampled radii, while unrelaxed NCC clusters have entropy profiles that flatten off in the core regions (e.g. Sanderson et al. 2006; Vikhlinin et al. 2006; Pratt et al. 2007; Arnaud et al. 2010) depending on a number of factors such as the temperature of the system and its dynamical state. In particular, hotter, more massive objects have a higher mean core entropy (e.g., Cavagnolo et al. 2009; Sanderson et al. 2009; Pratt et al. 2010).

Figure 8 shows the mean entropy radial profiles for the subsamples of relaxed and unrelaxed clusters in the NR, CSF and AGN runs. We compare these mean entropy profiles with the profiles from Eckert et al. (2013), who derived the thermodynamic properties of the intra-cluster gas (i.e., temperature and entropy) for a sample of 18 clusters by combining the SZ thermal pressure from *Planck* and the X-ray gas density from *ROSAT*. Based on the value of the central entropy (Cavagnolo et al. 2009), six of these clusters were classified as CC ($K_0 < 30$ keV cm²), while the remaining 12 are NCC.

Independently of the dynamical state of the systems, in outer

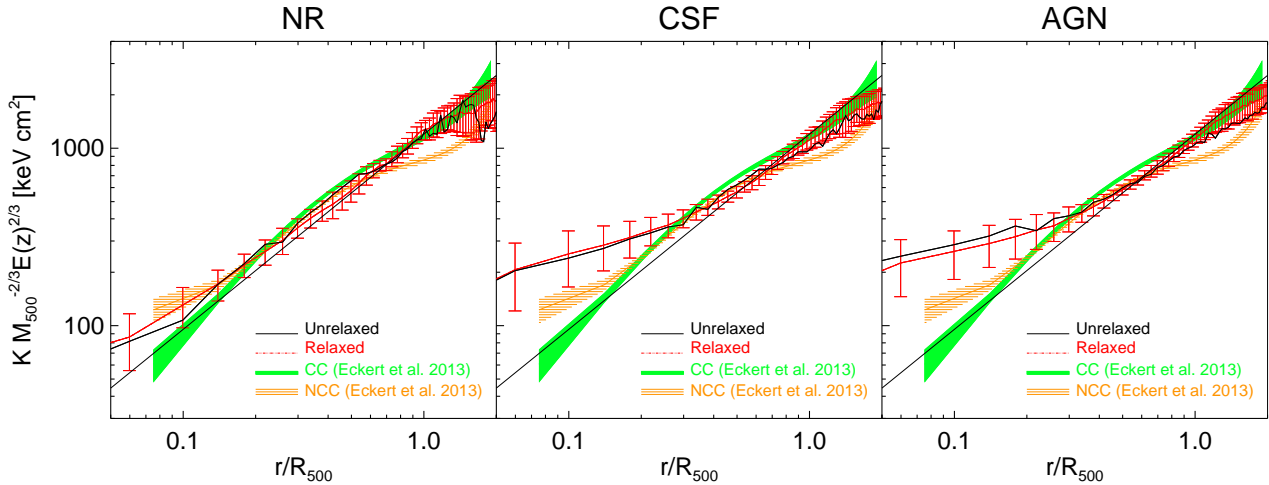


Figure 8. Mean entropy radial profiles at $z = 0$ for the sample of massive clusters in our NR (left panel), CSF (middle panel) and AGN (right panel) simulations. Mean profiles are computed separately for the unrelaxed and relaxed subsamples of simulated clusters (black continuous and red dotted-dashed lines, respectively). Error bars correspond to the 1σ scatter around the mean profile. We compare our results with the observed cluster entropy profiles by Eckert et al. (2013), which are represented by the coloured areas indicating the average scaled profile $\pm 1\sigma$ dispersion around it. The thinner solid black line in all panels shows for reference the $K \propto r^{1.1}$ profile.

cluster regions ($r \gtrsim 0.1R_{500}$), the slope of the entropy profiles of the simulated clusters in the NR set is consistent with the observed ones (and close to the $K \propto r^{1.1}$ scaling), although with a somewhat lower normalisation. At smaller radii there is more scatter both in observations and in simulations. At these radii, the entropy profiles of simulated clusters agree with those of the set of relaxed CC clusters analysed by Eckert et al. (2013), independently of their dynamical state.

As for the clusters in the CSF and AGN simulations, both relaxed and unrelaxed systems show entropy profiles that are also broadly consistent in slope with the theoretical self-similar scaling at large cluster-centric radii ($r \gtrsim 0.3 - 0.4 R_{500}$), thus supporting the idea that gravity dominates the ICM thermodynamics in outer cluster regions. For inner regions the slope of the profiles in simulations decreases and approaches that of the observed profiles of NCC clusters. Both in the CSF and in the AGN simulations the profiles for relaxed and unrelaxed systems are virtually identical. Therefore, although introducing star formation and feedback changes the entropy level in the central cluster regions, such effects are unable to create the observed diversity between CC and NCC systems. Furthermore, the similarity of the profiles obtained for the CSF and AGN simulations indicates that cooling is responsible for setting the entropy level below which gas cools and forms stars, while the nature and efficiency of feedback determines how much of this gas drops out of the hot phase.

3.3.3 Pressure profiles

The analysis of the temperature and entropy profiles demonstrates that clusters have a variety of behaviours in central regions, depending on the presence and prominence of cool cores (e.g. Pratt et al. 2010), but outside of core regions they behave as a more homogeneous population and follow the expectations of the self-similar model. A good illustration of the homogeneity of the ICM properties is represented by the pressure profiles.

In Fig. 9 we show the mean radial pressure profiles obtained for the sample of clusters in our three sets of simulations. The pressure profiles have been scaled by the ‘virial’ pressure P_{500} as

predicted by the hydrostatic equilibrium condition (see Nagai et al. 2007a):

$$P_{500} = 1.45 \times 10^{-11} \text{ erg cm}^{-3} \left(\frac{M_{500}}{10^{15} h^{-1} M_{\odot}} \right)^{2/3} E(z)^{8/3}. \quad (13)$$

In addition, in order to highlight the differences among the different physical models, they have been scaled as well by $(r/R_{500})^3$. With this scaling, the height of the pressure profiles corresponds to the contribution per radial interval to the total thermal energy content of the cluster (Battaglia et al. 2012a).

We compare our mean profiles with the X-ray observations of the *REXCESS* sample by Arnaud et al. (2010), and with the SZ data from Planck Collaboration et al. (2013). Planck Collaboration et al. (2013), taking advantage of the all-sky coverage and broad frequency range of the *Planck* satellite, studied the SZ pressure profiles of 62 nearby massive clusters detected at high significance in the 14-month nominal survey. Most of these clusters were individually detected at least out to R_{500} . Then, by stacking the radial profiles, they statistically detected the radial SZ signal out to $3R_{500}$.

From Fig. 9 we see that the effect on pressure profiles of radiative cooling, star formation and different forms of feedback is generally relatively small, with all simulation models agreeing rather well with observational results. To first order, pressure profiles should just reflect the condition of hydrostatic equilibrium within the potential wells that are established during the cosmological assembly of clusters, thus following a nearly universal profile (e.g. Nagai et al. 2007a; Arnaud et al. 2010). As such, they should be relatively insensitive to the details of the thermodynamical status of the ICM. This is the reason why mass proxies associated with pressure, such as the integrated Compton- y parameter or the aforementioned Y_X , are considered as robust mass proxies.

A closer look at Fig. 9 shows that radiative cooling creates a decrease of pressure with respect to the non-radiative case, at $r \lesssim 0.2R_{500}$. As a result, the average pressure profile for the NR case tends to be somewhat higher than the observed one. At these small radii the two radiative simulation sets produce results that are close to each other and in good agreement with both X-

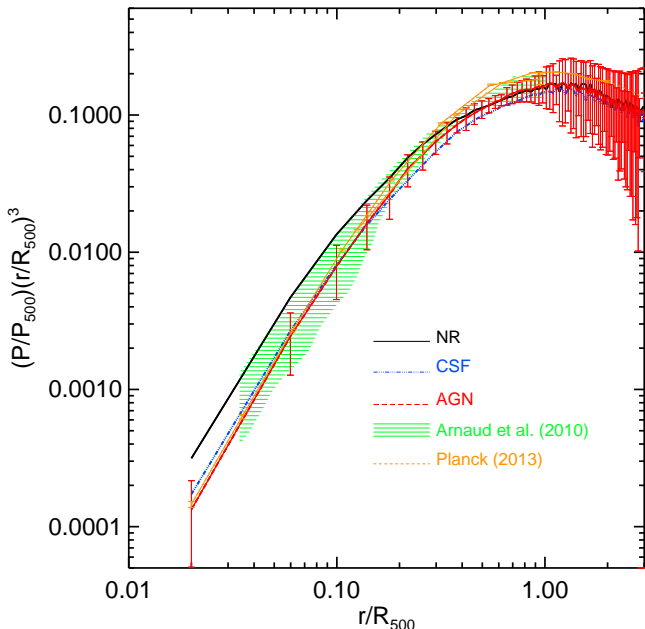


Figure 9. Mean pressure profiles (in units of P_{500}), for our sample of massive clusters with $T_{sl,500} > 3$ keV. In order to highlight the differences among the different physical models, these pressure profiles have been scaled by $(r/R_{500})^3$. Black continuous, blue dotted-dashed and red dashed lines stand for the mean profiles in the NR, CSF and AGN simulations, respectively. For the sake of clarity, error bars showing 1σ scatter are shown only for the AGN simulations. The green shadowy area corresponds to the average scaled profile $\pm 1\sigma$ dispersion around it as observed by Arnaud et al. (2010) from XMM observations, whereas the dashed orange line with error bars stands for the corresponding profile from SZ observations obtained by Planck Collaboration et al. (2013).

ray (Arnaud et al. 2010) and SZ (Planck Collaboration et al. 2013) data. Our result on the weak sensitivity of central pressure on the inclusion of AGN feedback apparently disagrees with the results presented by Battaglia et al. (2010). Using simulations also based on the SPH GADGET code, they showed instead that simulations with AGN feedback produce pressure profiles that, in core regions, are below those obtained without this feedback source. However, we note that, besides the differences in the implementation of the AGN feedback model, Battaglia et al. (2010) carried out simulations within cosmological boxes which are not large enough to include a significant population of the hot systems, with $T_{sl,500} > 3$ keV, considered in our analysis. As a result, their pressure profiles give more weight to the population of low-mass systems. In fact, we verified that restricting our analysis only to clusters and groups with $T_{sl,500} < 3$ keV, AGN feedback has the effect of decreasing pressure in central regions. Besides being in line with the findings of Battaglia et al. (2010), this result also agrees with the expectation that the total thermal content of the ICM is only weakly affected by feedback sources in massive systems while being more sensitive to feedback in systems with lower virial temperature.

A detailed comparison of the pressure profiles obtained in observations and those derived from simulations including different sets of physics would deserve a deeper study. Since this is beyond the scope of the present paper, we refer the reader to a future work (Planelles et al. in prep.) in which we will present a detailed analysis of the pressure profiles, along with a comparison with obser-

vational data, and a study of their dependence on mass, evolution with redshift and possible observational biases.

4 METAL ENRICHMENT OF THE ICM

The analysis of the content and distribution of metals within the intra-cluster medium provides direct means of understanding the interplay between the process of star formation, taking place on small scales within galaxies, and the feedback and gas-dynamical processes which determine the thermal properties of the ICM. While star formation affects the quantity of metals that are produced by different stellar populations, various feedback and dynamical processes affecting the gas (such as turbulent motions, ram-pressure and tidal stripping) are responsible for displacing the metals from star forming regions and determining their distribution in the ICM.

The model of chemical evolution included in our simulations (Tornatore et al. 2007) allows us to follow the production of heavy elements by accounting for the contributions from SN-II, SN-Ia and low and intermediate mass stars. Whether or not these metals will then be distributed throughout the ICM will depend on the competing roles of cooling of enriched gas, which causes metals to get locked in stars, and of feedback and gas-dynamical processes, which are responsible for the circulation of metals outside star-forming regions. In this Section we compare predictions of the ICM metal enrichment from the CSF and AGN simulations to observational data of galaxy clusters and groups. We present results on the relation between global metallicity and cluster mass, the Fe distribution and its corresponding abundance profile, and the relative abundance of Si with respect to Fe. Finally, we show how different feedback sources affect the relative metal enrichment of the diffuse hot gas and of the stellar component.

We refer to observational results from *Chandra*, *XMM-Newton* or *SUZAKU* for comparison. Before proceeding it is worth pointing out that simulated metal abundances can only be expected to match the observations to within a factor of ~ 2 (see also McCarthy et al. 2010), owing to the uncertainties in the underlying chemical evolution model, e.g. related to the adopted nucleosynthesis yields, the SN-Ia rates or the stellar lifetimes.

Throughout this Section, all metal abundances are scaled to the solar abundances provided by Grevesse and Sauval (1998). In addition, unless otherwise stated, we will rely on emission-weighted estimates of metal abundances (see Eq. 5). The emission-weighted estimator has been shown to reproduce quite closely the values obtained by fitting the X-ray spectra of simulated clusters, at least for Fe and Si (e.g., Kapferer et al. 2007; Rasia et al. 2008), whereas oxygen abundance may be significantly biased. In the case of oxygen, the difficulty of determining the continuum for the measurement of the line width and the weakness of the corresponding lines at high temperatures (e.g., Rasia et al. 2008) cause the emission-weighted estimator to seriously overestimate the corresponding abundance, especially for hot systems ($T \gtrsim 3$ keV).

Since a unique extraction radius is not defined for the observed catalogues, depending on the observational sample we compare with, we adopt either R_{500} or R_{180} as common extraction radii to compute metal abundances of simulated clusters. We verified that adopting a larger extraction radius (e.g. R_{vir}) instead slightly lowers the spectroscopic-like temperatures without changing substantially the results on the abundance (see as well Fabjan et al. 2008).

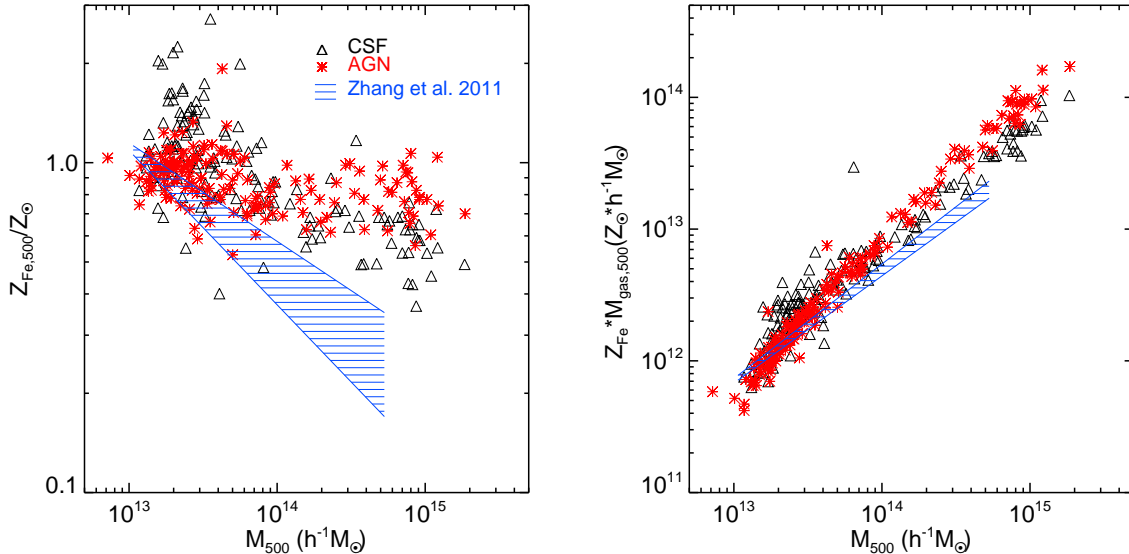


Figure 10. Emission-weighted iron abundance (left panel) and iron mass (right panel) within R_{500} as a function of M_{500} . Black triangles and red stars stand for the results from our CSF and AGN runs, respectively. Shaded blue area refers to the observational fitting obtained by Zhang et al. (2011).

4.1 The mass–metallicity relation

Figure 10 shows, for the sample of clusters within each of our radiative runs, the iron abundance (left panel) and iron mass (right panel) as a function of the mass within R_{500} . We compare these results with the observational sample by Zhang et al. (2011), who investigated the baryon mass content for a subsample of 19 clusters of galaxies extracted from the X-ray flux-limited sample HIFLUGCS. In their analysis, ICM metallicity and gas mass are based on *XMM-Newton* data, while they derived cluster masses from measurements of the “harmonic” velocity dispersion as described by Biviano et al. (2006).

The observational results by Zhang et al. (2011) indicate that less massive clusters, which have lower gas-mass fractions but higher iron-mass fractions, are more metal-rich. A plausible explanation for this result is that, in less massive galaxy clusters the star-formation efficiency is higher, that is, more stars were formed that have delivered more metals to enrich the hot gas. On the other hand, higher-mass clusters have a lower star-formation efficiency and less metal enrichment in the hot gas by stars, in part because feedback energy from, e.g., merging, is more efficient in quenching star formation in their member galaxies. In addition, given their deeper potential wells, a larger amount of hot gas is accreted in more massive clusters, diluting, therefore, the iron abundance more.

As we can infer from the analysis of Fig. 10, we obtain a mild decrease of Fe abundance with increasing total cluster mass (left panel), in agreement with the trends seen in previous analyses of simulations including chemical enrichment (e.g. Fabjan et al. 2008; Davé et al. 2008).

As for the effect of feedback on this relation, we note that the effect of including AGN is to weaken further the relation between iron abundance and cluster mass. On the scale of groups, $M_{500} \lesssim 10^{14} h^{-1} M_{\odot}$, AGN feedback decreases the iron abundance with respect to the CSF case, to a level more consistent with observations. For more massive systems, $M_{500} \gtrsim 10^{14} h^{-1} M_{\odot}$, AGN feedback has the opposite effect, thereby producing values of iron abundance higher by a factor of ~ 2 than in real clusters.

These trends stem from the differential effect that AGN feedback has on systems of different masses. In low-mass systems enriched gas is expelled at high redshift, thereby allowing metal poorer gas to be later accreted from the surrounding IGM. On the contrary, in more massive systems enriched gas is more efficiently retained within their potential wells. At the same time, suppression of star formation due to the action of AGN feedback allows the metal enriched gas to remain in the hot phase, instead of being locked in stars, thus increasing the overall enrichment level of the ICM.

The right panel of Fig. 10 also demonstrates that simulations with AGN feedback also provide the correct total iron mass at the scale of groups. This implies that these simulations provide both the correct amount of metals and the correct gas mass within low-mass systems. In general, more massive systems have too much iron mass.

Generally speaking, this result shows that our simulations do not produce the correct dependence of the ICM iron abundance on cluster mass. This is even more true for the AGN simulations, despite the fact that including AGN feedback generally provides a closer agreement with the observed thermal properties of the ICM (see Section 3). Ultimately, although our model of AGN feedback goes in the right direction of reducing BCG masses, it is not yet efficient enough to suppress star formation to the observed level at the centre of massive clusters. The resulting BCGs are still too massive (for a complete analysis see Ragone-Figueroa et al. 2013), and thus over-enrich the ICM to a too high level.

4.2 Radial profiles of iron abundance

The way in which metals are distributed in clusters carries information both on the past history of star formation and on the feedback and gas-dynamical processes which transport and diffuse them away from galaxies.

Figure 11 shows the mean emission-weighted iron abundance profiles obtained by averaging over the sample of hot ($T_{sl,500} \geq$

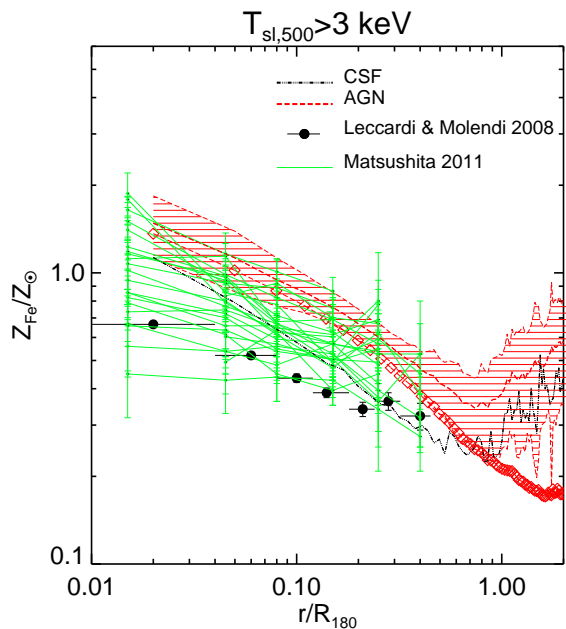


Figure 11. Mean emission-weighted iron abundance profiles for clusters with $T_{sl,500} \geq 3$ keV in our radiative simulations. Black dotted-dashed and red dashed lines stand for the CSF and AGN models, respectively. Red dashed line connected by diamond symbols shows the corresponding mean mass-weighted iron abundance profile for the clusters in the AGN set. For the sake of clarity, error bars showing 1σ scatter from the mean profile are shown only for the AGN run as a shaded area. Green error bars and filled circles with error bars show the observational results by Matsushita (2011) and Leccardi and Molendi (2008a), respectively.

3 keV) systems in our radiative simulations out to $2 \times R_{180}$. For completeness we overplot, only for the AGN run, the corresponding mean mass-weighted iron abundance profile.

We compare these with the observed metallicity profiles by Leccardi and Molendi (2008a) and Matsushita (2011). For the former, we show the combined profiles obtained from their analysis of about 50 clusters with $T \gtrsim 3$ keV, that were selected from the *XMM-Newton* archive in the redshift range $0.1 \leq z \leq 0.3$. Leccardi and Molendi (2008a) recovered metallicity profiles for these systems out to $\simeq 0.4R_{180}$. The results of this analysis show a central peak of Z_{Fe} , followed by a decline out to $0.2R_{180}$, while beyond that radius profiles are consistent with being flat, with $Z_{Fe} \simeq 0.3Z_{\odot}$, using the solar abundance value by Grevesse and Sauval (1998). As for Matsushita (2011), we show individual Fe abundance profiles of the 24 nearby ($z < 0.08$) clusters of galaxies observed with *XMM-Newton* included in their sample, that have an average ICM temperature above 3 keV. The results obtained from this study are in qualitative agreement with those found by Leccardi and Molendi (2008a) although with a slightly higher normalization.

The mean profile for the AGN case is slightly shallower than in the CSF case and with a higher normalization. The difference in shape is consistent with the expectation that AGN feedback is effective in redistributing metals within the ICM. Our mean profiles show the presence of abundance gradients in the central regions whose shape is in reasonable agreement with observational results. As discussed above, the higher enrichment level found in the AGN simulations is due to the efficiency with which this feedback model

is able to suppress star formation and displace metals from star forming regions, thereby preventing highly-enriched gas with short cooling time to be locked back into stars.

In general, the fact that simulations provide a shape of the metallicity profile which is similar to the observed ones should be regarded as a remarkable success of simulations. Changes to specific parts of the chemical evolution model, e.g. different sets of stellar yields (e.g., Tornatore et al. 2007; Wiersma et al. 2009); choice of the stellar IMF; a decrease in the fraction of binary systems, which are the progenitors of SNe-Ia (e.g., Fabjan et al. 2008), could be implemented to reduce the overall metal content, thus decreasing the normalization of the abundance profiles to the observed level.

At large radii our simulations show a pronounced increase of the Fe abundance up to the outermost radius with a relatively large scatter. As we will discuss below, this increase of the emission-weighted iron profile in outer cluster regions is due to the presence of halos containing highly-enriched gas which has not yet been ram-pressure stripped. Being at high density, this gas provides a strong contribution to the emission-weighted metallicity. This interpretation is confirmed by the comparison with the mass-weighted iron abundance profile which, instead, smoothly decreases out to the outermost sampled radii.

Our results in inner cluster regions are in general agreement with those obtained from previous simulations including different forms of energy feedback (e.g., Bhattacharya et al. 2008; Fabjan et al. 2010; McCarthy et al. 2010). However, none of these previous works show the steep increase of the emission-weighted iron abundance profiles that we find in outer cluster regions. Nevertheless, we need to be careful with this comparison since most of the results presented in the literature refer either to mass-weighted profiles or to profiles only for low-temperature systems (below 3 keV), for which we also see no such increase at large radii.

In order to better understand the shape of the emission-weighted Fe profiles at large radii, we show in Fig. 12 the maps of emission-weighted iron abundance for two different systems, in the CSF (left column) and AGN (right column) sets, respectively. These systems correspond to a galaxy cluster with $T_{sl,500} \sim 7$ keV (top row) and a smaller system with $T_{sl,500} \sim 1$ keV (bottom row). Each map has a side of length $2 \times R_{vir}$ and, therefore, they represent a region of $\sim 5h^{-1}$ Mpc for the big galaxy cluster and $\sim 1.6h^{-1}$ Mpc for the smaller one. We have also highlighted with white circles the values of R_{180} (solid line) and of R_{500} (dashed line) for both systems.

From a visual inspection of these maps we qualitatively appreciate the effect that different feedback mechanisms have on the ICM enrichment pattern. For the more massive system (top row), the distribution of Fe is quite different in the CSF and AGN cases. Despite the high efficiency that galactic winds have in spreading metals in the intergalactic medium at high redshifts ($z \gtrsim 2$; e.g., Oppenheimer and Davé 2008; Tornatore et al. 2010; Fabjan et al. 2010), winds in the CSF case are not efficient enough to regulate star formation inside clusters. As a result, within $\sim 0.5R_{180}$, a central high-metallicity peak is surrounded by a relatively low-metallicity gas, partially stripped by merging galaxies. In the outer cluster regions highly-enriched gas clumps are still present. As explained above, these clumps are responsible for the increase of the emission-weighted iron abundance profiles at large radii, shown in Fig. 11. From the top-right panel of Fig. 12 we infer that AGN feedback has higher efficiency in mixing and distributing the metals through the ICM. As a result, instead of a clumpy distribution of

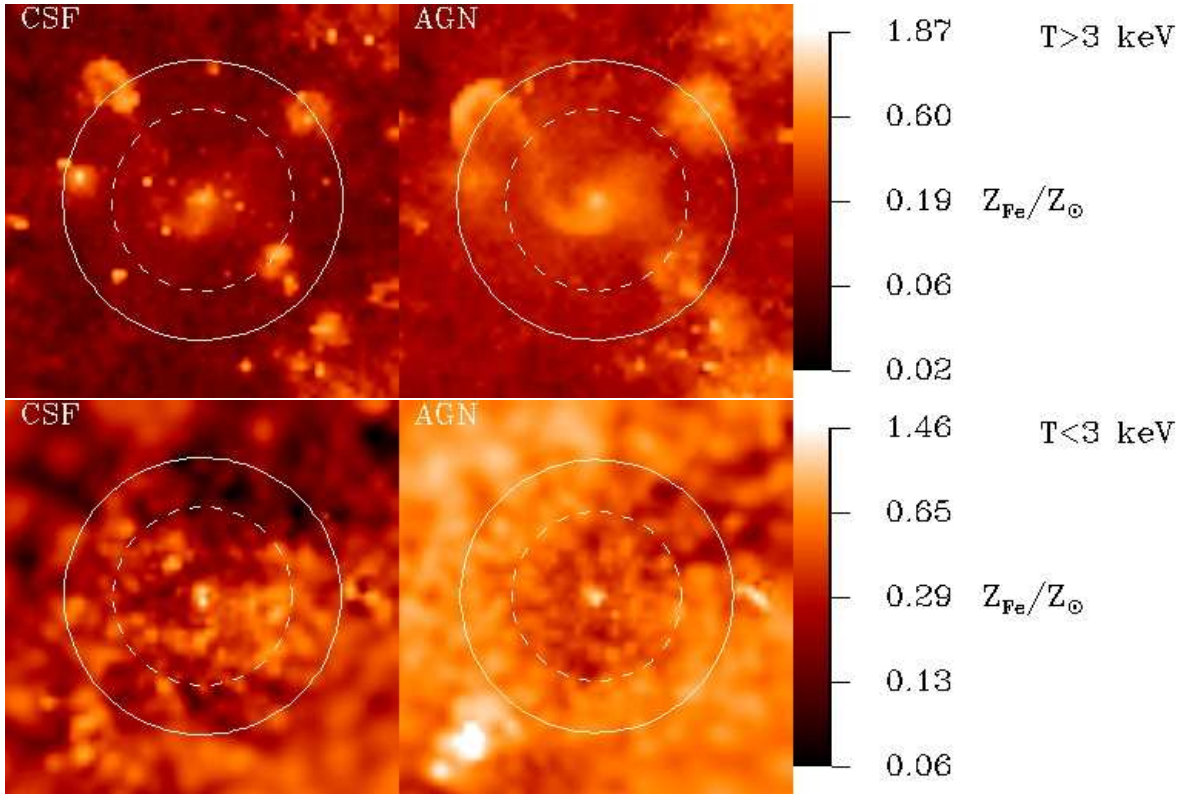


Figure 12. Maps of emission-weighted iron abundance for two different systems in the CSF (left column) and AGN (right column) simulation sets, respectively. In the top row the maps are shown for a galaxy cluster with $M_{500} \sim 9 \times 10^{14} h^{-1} M_{\odot}$, $T_{sl,500} \sim 7 \text{ keV}$ and $R_{vir} \sim 2.5 h^{-1} \text{ Mpc}$, whereas in the bottom row a group with $M_{500} \sim 3 \times 10^{13} h^{-1} M_{\odot}$, $T_{sl,500} \sim 1 \text{ keV}$ and $R_{vir} \sim 0.85 h^{-1} \text{ Mpc}$ is represented. Abundance values are expressed in units of the solar values, as reported by Grevesse and Sauval (1998), with colour coding specified in the right bar. For each object, each map has a side of $2 \times R_{vir}$. White circles on each panel represent the values of R_{180} (continuous line) and R_{500} (dashed line) for both systems. We have normalized the values of Fe abundance to a common maximum and minimum values in order to make comparable the different runs for the same system.

highly-enriched gas, we obtain a rather high level of diffuse enrichment from the centre to the outskirts. Within the virial radius of the cluster, the transition between the enrichment of the central Fe peak and the surroundings is more continuous than in the CSF case, thus giving rise to shallower profiles. For outer cluster regions, although highly-enriched regions in the outskirts are more diluted than in the previous case, they contribute in the same way to the slope of the iron abundance profiles.

The situation is completely different for the smaller system (bottom row). In this case the level of enrichment of the ICM decreases from the highly-enriched central core out to the outermost regions in both radiative runs, although the values of Z_{Fe} are slightly higher in the case of the AGN simulation throughout the cluster volume. In addition, given the efficiency of AGN feedback in spreading metals from star-forming regions, the iron distribution is much more uniform in this case, thus producing flatter Z_{Fe} profiles in outer regions (see also Fabjan et al. 2010).

The sensitivity of the metal distribution in cluster outskirts on the nature of feedback demonstrates the relevance of pushing observational analyses of the ICM enrichment out to large radii. While carrying out such measurements well outside R_{500} is beyond the reach of the current generation of X-ray telescopes, the future generation of high-sensitivity instruments, with both large collecting area and high spectral and angular resolution, would be able to trace the pattern of ICM chemical enrichment out to such radii, thereby constraining the past history of cosmic feedback.

4.2.1 The Z_{Si}/Z_{Fe} relative abundance

SNe-Ia produce a large amount of Fe and Ni elements, while SNe-II are the main contributors of O, Ne, and Mg. Si-group elements (Si, S, Ar, and Ca) are produced by both SN types in similar proportions. Therefore, studying the relative abundance of different elements potentially offers a means to infer the relative contribution of different stellar populations to the ICM enrichment and, subsequently, to reconstruct the stellar IMF (e.g. Loewenstein 2013, and references therein).

Early ASCA data (e.g., Loewenstein and Mushotzky 1996; Fukazawa et al. 1998; Finoguenov et al. 2000) suggested that cluster outskirts are predominantly enriched by SNe-II. A similar result was found more recently by Rasmussen and Ponman (2007) and Rasmussen and Ponman (2009). These authors analysed *XMM-Newton* data for poor clusters with $T \lesssim 3 \text{ keV}$ obtaining rather flat profiles of Z_{Si}/Z_{Fe} with a value close to solar at small radii, followed by a steep rise beyond $\sim 0.2 R_{500}$. *SUZAKU* observations of low temperature clusters and groups (e.g., Sato et al. 2010; Sakuma et al. 2011; Matsushita et al. 2013, and references therein) show instead rather flat profiles of Z_{Si}/Z_{Fe} out to large radii, $\simeq 0.3 R_{vir}$, thus implying that SNe-Ia and SNe-II should contribute in similar proportions to the enrichment at different radii.

Figure 13 shows the mean emission-weighted Z_{Si}/Z_{Fe} radial profiles for our sample of high-temperature systems. As in previous simulations (e.g., Fabjan et al. 2010; McCarthy et al. 2010), we

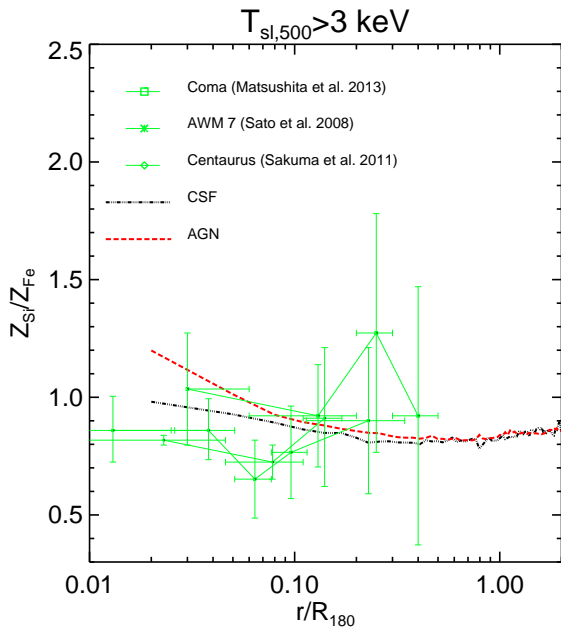


Figure 13. Mean emission-weighted $Z_{\text{Si}}/Z_{\text{Fe}}$ profiles obtained by averaging over simulated clusters with $T_{\text{sl},500} \geq 3$ keV. Black dotted-dashed and red dashed lines stand for the CSF and AGN runs, respectively. In order to compare with observational results, we use profiles from different *SUZAKU* observations.

find that Si/Fe abundance ratio is nearly flat as a function of radius from roughly $\sim 0.1R_{180}$ out to the outermost radius. Our results are qualitatively in good agreement with different *SUZAKU* observations (e.g., Sato et al. 2008; Sakuma et al. 2011; Matsushita et al. 2013), although within fairly large uncertainties. Simulations with AGN feedback produce a relative increase of the Si abundance in the central regions (see also Fabjan et al. 2010). This increase is due to the selective removal of metal-enriched gas associated with radiative cooling. Total metallicity of the gas around the BCG is dominated by SNe-II products. Therefore, gas more enriched by SNe-II has a relatively shorter cooling time. As a consequence, suppression of cooling in the core regions by AGN feedback tends to increase the amount of SN-II products in the ICM, thereby justifying the increase of $Z_{\text{Si}}/Z_{\text{Fe}}$ with respect to the CSF runs.

A central relative enhancement of silicon abundance, as found in the AGN case, is marginally disfavoured by available observations. This may hint at a lack of some diffusion or transport process in our simulations, which are responsible for mixing different metal species. In our simulations, the effect of AGN is to provide a purely thermal feedback. In this respect, the explicit inclusion of kinetic feedback in the form of sub-relativistic jets is expected to trigger turbulence and circulation of gas which may have a significant effect on the distribution of metals in central cluster regions.

4.3 Metallicity of stars

Given the significant suppression of star formation in the simulations including AGN feedback, it may appear surprising that these simulations are characterized by a higher level of ICM enrichment. In fact, the explanation for this behaviour lies in the different efficiency with which metals, after being distributed from star particles to the surrounding gas particles, are later locked back into stars.

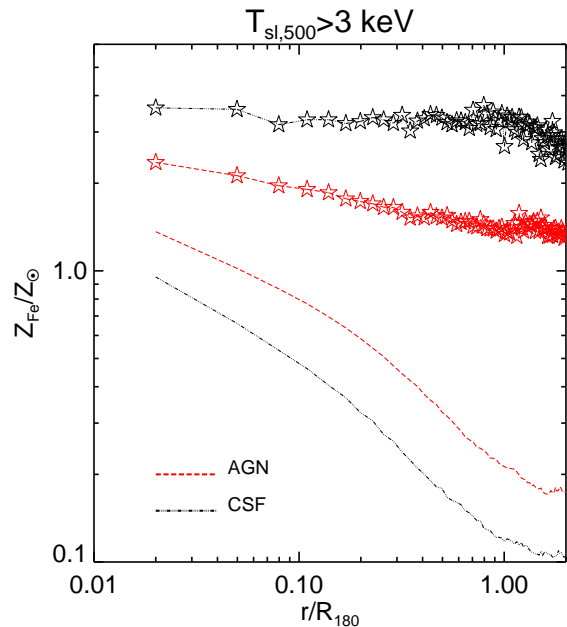


Figure 14. Mean mass-weighted iron abundance profiles for the gas and the stellar components in our CSF and AGN runs. Black dotted-dashed and red dashed lines represent the Z_{Fe} in gas of the CSF and AGN runs, respectively. The same type of lines connected by star symbols represent the corresponding Z_{Fe} in the stellar component for each run. These profiles have been obtained by averaging over the sample of hot systems with $T_{\text{sl},500} \geq 3$ keV out to $2 \times R_{180}$.

Figure 14 compares the mean mass-weighted iron abundance profiles (already displayed in Fig. 11) together with the corresponding mean profiles for the iron abundance in stars. A comparison between the two simulations shows nearly an order of magnitude difference in the normalization of the mean profiles associated with the stellar component, with the CSF run being much more metal rich than those in the AGN run. The effect of feedback from SMBHs is therefore not only to quench the overall star formation rate, but also to prevent highly-enriched gas particles, which have a short cooling time, from undergoing rapid star formation. BHs heat the surrounding gas causing it to expand out of the dense, star-forming regions, thereby raising the fraction of the total metal mass in the gas phase. The efficient ejection of metals from star-forming regions is the mechanism by which the AGN simulations yield ICM metal abundances similar to, or even larger than, those in the CSF case, in spite of a stellar mass fraction that is ~ 3 times smaller (see also Sijacki et al. 2007; Fabjan et al. 2010; McCarthy et al. 2010; Planelles et al. 2013).

These results highlight that the nature of feedback affects not only the star formation within cluster galaxies, but also the way in which metals are distributed between the hot ICM and stars. Independent analyses based on semi-analytical models of galaxy formation (e.g., De Lucia and Borgani 2012; Henriques et al. 2013) have in fact demonstrated that the metal content of galaxies, and most prominently of the BCGs, are inextricably linked to the past history of star formation and provide quite stringent constraints on the nature of feedback. A complete analysis of the properties of the galaxy population in simulations will be presented in a future analysis.

5 SUMMARY AND DISCUSSION

We have analysed a set of cosmological hydrodynamical simulations of galaxy clusters paying special attention to the effects that different implementations of baryonic physics have on the thermal and chemodynamical properties of these systems. Using the Tree-PM SPH code `GADGET-3` (Springel 2005), we carried out re-simulations of 29 Lagrangian regions extracted around as many galaxy clusters identified within a low-resolution N-body parent simulation. These cluster re-simulations have been performed using different prescriptions for the baryonic physics: without including any radiative processes (NR runs), including the effect of cooling, star formation and SN feedback (CSF runs), and including also an additional contribution from an efficient model of AGN feedback (AGN runs).

The final sample of objects obtained within each one of these sets of re-simulations consists of $\simeq 160$ galaxy clusters and groups with $M_{vir} \geq 3 \times 10^{13} h^{-1} M_{\odot}$ at $z = 0$. Using these three sets of simulated galaxy clusters, we have analysed how star formation and feedback in energy and metals from SN and AGN affect their X-ray scaling relations and associated radial profiles, and the chemical enrichment pattern of their hot intra-cluster gas. Our main results can be summarised as follows.

- Including gas accretion onto SMBH and the ensuing AGN feedback provides, in general, a better agreement between simulation results and observations of X-ray scaling relations. The differential effect that AGN feedback has at the scales of groups and of massive clusters is such to change the slope and normalization of the mass-temperature relation and bring it into better agreement with observational results with respect to the NR and CSF cases. In a similar way, injection of entropy from AGN feedback causes a suppression of gas density at the centre of groups, relative to clusters, thereby bringing the L_X - T_{sl} and K - T_{sl} relations into closer agreement with observations (see also Puchwein et al. 2008; Short et al. 2010; Fabjan et al. 2010; McCarthy et al. 2010).

- Feedback also has an impact on the thermal structure of the ICM and, in turn, on the difference between mass-weighted and spectroscopic-like temperature, the latter being sensitive to the presence of clumps of relatively cold gas associated with substructures, from which it is eventually ram-pressure stripped. Removal of cold gas in substructures by radiative cooling or by the effect of efficient AGN feedback goes in the direction of decreasing the thermal complexity of the ICM and, therefore, the difference between T_{mw} and T_{sl} . A careful comparison with observations on the temperature distribution of the ICM (e.g. Frank et al. 2013) is required in order to verify whether our simulations provide the correct degree of thermal complexity in clusters.

- Simulations including AGN feedback recover both X-ray and SZ results on the pressure profiles quite well. Although we also find a reasonable agreement with observations of temperature and entropy profiles, our simulations do not produce the observed difference in profiles between relaxed, cool-core clusters and unrelaxed, non cool-core systems, even when AGN feedback is included. We regard this as a major limitation of the implementation of AGN feedback included in our simulations. Ultimately, this traces back to the limited capability of current implementations of AGN feedback in cosmological simulations to produce the correct structure of cool cores.

- In broad agreement with observations (e.g., Zhang et al. 2011), we obtain a decreasing iron abundance with increasing total cluster mass. However, observational data reveals a decrease of iron abundance in high-mass systems that is stronger than pre-

dicted by our simulations. Such a difference is even worsened by the inclusion of AGN feedback. In this case, highly-enriched gas in massive clusters is prevented from cooling out of the hot phase, thereby increasing the enrichment level with respect to simulations including only SN feedback. This tension is caused by the still insufficient regulation of star formation provided by simulated AGN feedback at the centre of massive halos (e.g. Puchwein and Springel 2013), which also causes simulated BCGs to be too massive with respect to the observed ones (for a detailed analysis see Ragone-Figueroa et al. 2013, and references therein).

- Despite the exceedingly high level of iron abundance predicted in massive clusters, the shape of the radial profiles of Fe abundance is in better agreement with the observed profiles when AGN feedback is included. In general, we find that AGN produces a higher and much more widespread pattern of metal enrichment in the outer part of galaxy clusters and groups. In fact, AGN feedback, combined with galactic winds, is quite efficient in ejecting highly-enriched gas from star-forming regions, thus enhancing the metal circulation in the inter-galactic medium. This generates a rather uniform and widespread pattern of metal enrichment in the outskirts of clusters.

- Our simulations predict almost flat profiles of Z_{Si}/Z_{Fe} out to the outermost radii. Suppression of star formation in the runs with AGN feedback causes Z_{Si}/Z_{Fe} to increase at small radii, $\lesssim 0.1 R_{500}$, a feature which is possibly in tension with the rather uncertain observational results. If confirmed, this tension may suggest that some additional mechanisms, not included in our simulations, are responsible for efficient mixing of metals in the central cluster regions.

- Despite the suppression of star formation in the AGN simulations, they produce a higher level of enrichment in massive clusters. The reason for this apparently paradoxical result is that AGN feedback is efficient in preventing highly-enriched gas to leave the hot phase and form stars. As a result, we consistently find stellar metallicity in the AGN simulations to be suppressed by almost a factor of 2 with respect to the CSF case.

Our results support the idea that including feedback from SMBHs significantly improves the ability of cosmological hydrodynamical simulations to yield a realistic population of galaxy clusters and groups. Indeed, this result agrees qualitatively with previous works that implemented BH growth and feedback in cosmological simulations of galaxy clusters and groups (e.g., Sijacki et al. 2007; Puchwein et al. 2008; Fabjan et al. 2010; McCarthy et al. 2010). These findings are quite encouraging, especially if we keep in mind that relatively simple prescriptions are adopted to describe the rate of gas accretion and the thermalisation of the extracted energy. An interesting prediction of these simulations is that the pattern of metal distribution in the cluster outskirts represent a fossil record of the interplay between feedback and star formation during the hierarchical assembly of clusters. While tracing the enrichment of the inter-galactic medium in this regime is beyond the capabilities of the available X-ray telescopes, future instruments are expected to have the required sensitivity and spectroscopic capability, thereby shedding light on a crucial aspect of galaxy evolution.

Despite the above successes, our results also highlight that a number of discrepancies between observations and predictions from simulations still exist. Even including AGN feedback we are not able to produce the correct cooling/heating interplay in cluster cores. This limitation manifests itself in, e.g., BCGs that are too large and the lack of diversity of ICM properties between relaxed and unrelaxed systems.

One aspect of our AGN implementation that needs to be improved is related to the pure thermal nature of the associated feedback. Observational results indicate that sub-relativistic jets from the BH hosted in central cluster galaxies shocks the surrounding ICM, thereby producing bubbles of high-entropy gas. Controlled numerical experiments of isolated clusters (e.g. Omma et al. 2004; Brighenti and Mathews 2006; Gaspari et al. 2011) and disk galaxies, or controlled galaxy mergers (Choi et al. 2012; Barai et al. 2013) have already demonstrated that kinetic AGN feedback provides results that are rather different from those based on thermal feedback. In particular, outflows generate circulation of gas that has the twofold effect of stabilising cooling flows and distributing enriched gas outside the innermost regions. Including mechanical AGN feedback in cosmological simulations is clearly a step to be undertaken (e.g. Martizzi et al. 2012), along with the exploration of accretion models different from the standard Bondi criterion.

ACKNOWLEDGEMENTS

The authors would like to thank Volker Springel for making available to us the non-public version of the GADGET-3 code and Annalisa Bonafede for her help with generating the initial conditions for the simulations. We also would like to thank Gabriel Pratt, Dominique Eckert and Kyoko Matsushita for supplying us with observational data to compare with, and the anonymous referee for his/her constructive comments that helped improving the presentation of the results. Simulations have been carried out at the CINECA supercomputing Centre in Bologna, with CPU time assigned through ISCRAs proposals and through an agreement with University of Trieste. SP and MK acknowledge a fellowship from the European Commission's Framework Programme 7, through the Marie Curie Initial Training Network CosmoComp (PITN-GA-2009-238356). DF acknowledges founding from the Centre of Excellence for Space Sciences and Technologies SPACE-SI, an operation partly financed by the European Union, European Regional Development Fund and Republic of Slovenia, Ministry of Higher Education, Science and Technology. CR-F acknowledges founding from the Consejo Nacional de Investigaciones Científicas y Técnicas de la República Argentina (CONICET) and the Secretaría de Ciencia y Técnica de la Universidad Nacional de Córdoba - Argentina (SeCyT). This work has been supported by the PRIN-INAF09 project "Towards an Italian Network for Computational Cosmology", by the PRIN-MIUR09 "Tracing the growth of structures in the Universe", and by the PD51 INFN grant. This work has been partially supported by *Spanish Ministerio de Ciencia e Innovación* (MICINN) (grants AYA2010-21322-C03-02 and CONSOLIDER2007-00050).

REFERENCES

- Arnaud M., Evrard A.E., 1999, MNRAS, 305, 631
 Arnaud M., Pointecouteau E., Pratt G.W., 2007, A&A, 474, L37
 Arnaud M., Pratt G.W., Piffaretti R., Böhringer H., Croston J.H., Pointecouteau E., 2010, A&A, 517, A92
 Baldi A., Ettori S., Mazzotta P., Tozzi P., Borgani S., 2007, ApJ, 666, 835
 Balogh M.L., Pearce F.R., Bower R.G., Kay S.T., 2001, MNRAS, 326, 1228
 Balsara D.S., 1995, Journal of Computational Physics, 121, 357
 Barai P., Viel M., Murante G., Gaspari M., Borgani S., 2013, ArXiv e-prints
 Battaglia N., Bond J.R., Pfrommer C., Sievers J.L., Sijacki D., 2010, ApJ, 725, 91
 Battaglia N., Bond J.R., Pfrommer C., Sievers J.L., 2012a, ApJ, 758, 75
 Battaglia N., Bond J.R., Pfrommer C., Sievers J.L., 2012b, ArXiv e-prints
 Bhattacharya S., Di Matteo T., Kosowsky A., 2008, MNRAS, 389, 34
 Biviano A., Murante G., Borgani S., Diaferio A., Dolag K., Girardi M., 2006, A&A, 456, 23
 Böhringer H., Matsushita K., Churazov E., Ikebe Y., Chen Y., 2002, A&A, 382, 804
 Böhringer H., et al., 2000, ApJS, 129, 435
 Böhringer H., et al., 2004, A&A, 425, 367
 Böhringer H., et al., 2007, A&A, 469, 363
 Bonafede A., Dolag K., Staszczyn F., Murante G., Borgani S., 2011, MNRAS, 418, 2234
 Bondi H., 1952, MNRAS, 112, 195
 Booth C.M., Schaye J., 2009, MNRAS, 398, 53
 Borgani S., Kravtsov A., 2009, ArXiv e-prints
 Borgani S., Governato F., Wadsley J., Menci N., Tozzi P., Lake G., Quinn T., Stadel J., 2001, ApJL, 559, L71
 Borgani S., Fabjan D., Tornatore L., Schindler S., Dolag K., Diaferio A., 2008, Space Sci Rev, 134, 379
 Borgani S., et al., 2004, MNRAS, 348, 1078
 Borgani S., et al., 2006, MNRAS, 367, 1641
 Bower R.G., Benson A.J., Malbon R., Helly J.C., Frenk C.S., Baugh C.M., Cole S., Lacey C.G., 2006, MNRAS, 370, 645
 Bower R.G., McCarthy I.G., Benson A.J., 2008, MNRAS, 390, 1399
 Brighenti F., Mathews W.G., 2006, ApJ, 643, 120
 Bryan G.L., Norman M.L., 1998, ApJ, 495, 80
 Carlstrom J.E., Holder G.P., Reese E.D., 2002, ARA&A, 40, 643
 Cavagnolo K.W., Donahue M., Voit G.M., Sun M., 2009, ApJS, 182, 12
 Chabrier G., 2003, PASP, 115, 763
 Chen Y., Reiprich T.H., Böhringer H., Ikebe Y., Zhang Y.Y., 2007, A&A, 466, 805
 Choi E., Ostriker J.P., Naab T., Johansson P.H., 2012, ApJ, 754, 125
 Churazov E., Brüggem M., Kaiser C.R., Böhringer H., Forman W., 2001, ApJ, 554, 261
 Crone M.M., Evrard A.E., Richstone D.O., 1996, ApJ, 467, 489
 Cui W., Monaco G.M.P., Borgani S., Granato G.L., Killedear M., De Lucia G., Presotto V., Dolag K., 2013, ArXiv e-prints
 Davé R., Oppenheimer B.D., Sivanandam S., 2008, MNRAS, 391, 110
 De Grandi S., Molendi S., 2002, ApJ, 567, 163
 De Grandi S., Ettori S., Longhetti M., Molendi S., 2004, A&A, 419, 7
 De Lucia G., Borgani S., 2012, MNRAS, 426, L61
 de Plaa J., et al., 2006, A&A, 452, 397
 Di Matteo T., Springel V., Hernquist L., 2005, Nature, 433, 604
 Dubois Y., Devriendt J., Teyssier R., Slyz A., 2011, MNRAS, 417, 1853
 Eckert D., Molendi S., Vazza F., Ettori S., Paltani S., 2013, A&A, 551, A22
 Eckmiller H.J., Hudson D.S., Reiprich T.H., 2011, A&A, 535, A105
 Eke V.R., Cole S., Frenk C.S., 1996, MNRAS, 282, 263

- Ettori S., Dolag K., Borgani S., Murante G., 2006, *MNRAS*, 365, 1021
- Evrard A.E., 1990, *ApJ*, 363, 349
- Fabjan D., Tornatore L., Borgani S., Saro A., Dolag K., 2008, *MNRAS*, 386, 1265
- Fabjan D., Borgani S., Tornatore L., Saro A., Murante G., Dolag K., 2010, *MNRAS*, 401, 1670
- Fabjan D., Borgani S., Rasia E., Bonafede A., Dolag K., Murante G., Tornatore L., 2011, *MNRAS*, 416, 801
- Ferland G.J., Korista K.T., Verner D.A., Ferguson J.W., Kingdon J.B., Verner E.M., 1998, *PASP*, 110, 761
- Finoguenov A., David L.P., Ponman T.J., 2000, *ApJ*, 544, 188
- Frank K.A., Peterson J.R., Andersson K., Fabian A.C., Sanders J.S., 2013, *ApJ*, 764, 46
- Fukazawa Y., Makishima K., Tamura T., Ezawa H., Xu H., Ikebe Y., Kikuchi K., Ohashi T., 1998, *PASJ*, 50, 187
- Gaspari M., Melioli C., Brighenti F., D'Ercole A., 2011, *MNRAS*, 411, 349
- Giodini S., Lovisari L., Pointecouteau E., Ettori S., Reiprich T.H., Hoekstra H., 2013, *ArXiv e-prints*
- Granato G.L., De Zotti G., Silva L., Bressan A., Danese L., 2004, *ApJ*, 600, 580
- Grevesse N., Sauval A.J., 1998, *Space Sci Rev*, 85, 161
- Haardt F., Madau P., 2001, in D.M. Neumann, J.T.V. Tran, eds., *Clusters of Galaxies and the High Redshift Universe Observed in X-rays*
- Hasselfield M., et al., 2013, *Journal of Cosmology and Astroparticle Physics*, 7, 008
- Henriques B.M.B., White S.D.M., Thomas P.A., Angulo R.E., Guo Q., Lemson G., Springel V., 2013, *MNRAS*, 431, 3373
- Kaiser N., 1986, *MNRAS*, 222, 323
- Kapferer W., Kronberger T., Weratschnig J., Schindler S., 2007, *A&A*, 472, 757
- Kay S.T., Pearce F.R., Frenk C.S., Jenkins A., 2002, *MNRAS*, 330, 113
- Kay S.T., da Silva A.C., Aghanim N., Blanchard A., Liddle A.R., Puget J.L., Sadat R., Thomas P.A., 2007, *MNRAS*, 377, 317
- Kay S.T., Peel M.W., Short C.J., Thomas P.A., Young O.E., Battye R.A., Liddle A.R., Pearce F.R., 2012, *MNRAS*, 422, 1999
- Kravtsov A.V., Borgani S., 2012, *ARA&A*, 50, 353
- Kravtsov A.V., Yepes G., 2000, *MNRAS*, 318, 227
- Kravtsov A.V., Nagai D., Vikhlinin A.A., 2005, *ApJ*, 625, 588
- Kravtsov A.V., Vikhlinin A., Nagai D., 2006, *ApJ*, 650, 128
- Leccardi A., Molendi S., 2008a, *A&A*, 487, 461
- Leccardi A., Molendi S., 2008b, *A&A*, 486, 359
- Loewenstein M., 2013, *ApJ*, 773, 52
- Loewenstein M., Mushotzky R.F., 1996, *ApJ*, 466, 695
- Loken C., Norman M.L., Nelson E., Burns J., Bryan G.L., Motl P., 2002, *ApJ*, 579, 571
- Mahdavi A., Hoekstra H., Babul A., Bildfell C., Jeltema T., Henry J.P., 2013, *ApJ*, 767, 116
- Markevitch M., 1998, *ApJ*, 504, 27
- Martizzi D., Teyssier R., Moore B., 2012, *MNRAS*, 420, 2859
- Matsushita K., 2011, *A&A*, 527, A134
- Matsushita K., Sato T., Sakuma E., Sato K., 2013, *PASJ*, 65, 10
- Maughan B.J., 2007, *ApJ*, 668, 772
- Mazzotta P., Rasia E., Moscardini L., Tormen G., 2004, *MNRAS*, 354, 10
- McCarthy I.G., Schaye J., Bower R.G., Ponman T.J., Booth C.M., Dalla Vecchia C., Springel V., 2011, *MNRAS*, 412, 1965
- McCarthy I.G., et al., 2010, *MNRAS*, 406, 822
- McNamara B.R., Nulsen P.E.J., 2007, *ARA&A*, 45, 117
- Moll R., et al., 2007, *A&A*, 463, 513
- Monaghan J.J., 1997, *Journal of Computational Physics*, 136, 298
- Nagai D., Kravtsov A.V., Vikhlinin A., 2007a, *ApJ*, 668, 1
- Nagai D., Vikhlinin A., Kravtsov A.V., 2007b, *ApJ*, 655, 98
- Navarro J.F., Frenk C.S., White S.D.M., 1995, *MNRAS*, 275, 720
- Newton R.D.A., Kay S.T., 2013, *ArXiv e-prints*
- Omma H., Binney J., Bryan G., Slyz A., 2004, *MNRAS*, 348, 1105
- Oppenheimer B.D., Davé R., 2008, *MNRAS*, 387, 577
- Osmond J.P.F., Ponman T.J., 2004, *MNRAS*, 350, 1511
- Padovani P., Matteucci F., 1993, *ApJ*, 416, 26
- Peterson J.R., et al., 2001, *A&A*, 365, L104
- Plage T.J., et al., 2013, *ApJ*, 770, 112
- Planck Collaboration, et al., 2011, *A&A*, 536, A10
- Planck Collaboration, et al., 2013, *A&A*, 550, A131
- Planelles S., Quilis V., 2009, *MNRAS*, 399, 410
- Planelles S., Borgani S., Dolag K., Ettori S., Fabjan D., Murante G., Tornatore L., 2013, *MNRAS*, 431, 1487
- Power C., Knebe A., Knollmann S.R., 2012, *MNRAS*, 419, 1576
- Pratt G.W., Böhringer H., Croston J.H., Arnaud M., Borgani S., Finoguenov A., Temple R.F., 2007, *A&A*, 461, 71
- Pratt G.W., Croston J.H., Arnaud M., Böhringer H., 2009, *A&A*, 498, 361
- Pratt G.W., et al., 2010, *A&A*, 511, A85
- Puchwein E., Springel V., 2013, *MNRAS*, 428, 2966
- Puchwein E., Sijacki D., Springel V., 2008, *ApJL*, 687, L53
- Puchwein E., Springel V., Sijacki D., Dolag K., 2010, *MNRAS*, 406, 936
- Ragone-Figueroa C., Granato G.L., Murante G., Borgani S., Cui W., 2013, *ArXiv e-prints*
- Rasia E., Mazzotta P., Bourdin H., Borgani S., Tornatore L., Ettori S., Dolag K., Moscardini L., 2008, *ApJ*, 674, 728
- Rasia E., et al., 2012, *New Journal of Physics*, 14, 055018
- Rasmussen J., Ponman T.J., 2007, *MNRAS*, 380, 1554
- Rasmussen J., Ponman T.J., 2009, *MNRAS*, 399, 239
- Raymond J.C., Smith B.W., 1977, *ApJS*, 35, 419
- Reichardt C.L., et al., 2013, *ApJ*, 763, 127
- Reiprich T.H., Böhringer H., 2002, *ApJ*, 567, 716
- Renzini A., Ciotti L., D'Ercole A., Pellegrini S., 1993, *ApJ*, 419, 52
- Sakuma E., Ota N., Sato K., Sato T., Matsushita K., 2011, *PASJ*, 63, 979
- Sanderson A.J.R., Ponman T.J., O'Sullivan E., 2006, *MNRAS*, 372, 1496
- Sanderson A.J.R., O'Sullivan E., Ponman T.J., 2009, *MNRAS*, 395, 764
- Sato K., Matsushita K., Ishisaki Y., Yamasaki N.Y., Ishida M., Sasaki S., Ohashi T., 2008, *PASJ*, 60, 333
- Sato K., Kawaharada M., Nakazawa K., Matsushita K., Ishisaki Y., Yamasaki N.Y., Ohashi T., 2010, *PASJ*, 62, 1445
- Sembolini F., Yepes G., De Petris M., Gottloeber S., Lamagna L., Comis B., 2012, *ArXiv e-prints*
- Short C.J., Thomas P.A., Young O.E., Pearce F.R., Jenkins A., Muanwong O., 2010, *MNRAS*, 408, 2213
- Sijacki D., Springel V., 2006, *MNRAS*, 366, 397
- Sijacki D., Springel V., Di Matteo T., Hernquist L., 2007, *MNRAS*, 380, 877
- Snowden S.L., Mushotzky R.F., Kuntz K.D., Davis D.S., 2008, *A&A*, 478, 615
- Springel V., 2005, *MNRAS*, 364, 1105
- Springel V., Hernquist L., 2002, *MNRAS*, 333, 649
- Springel V., Hernquist L., 2003, *MNRAS*, 339, 289

- Springel V., White M., Hernquist L., 2001, *ApJ*, 549, 681
Springel V., Di Matteo T., Hernquist L., 2005, *MNRAS*, 361, 776
Stanek R., Rasia E., Evrard A.E., Pearce F., Gazzola L., 2010, *ApJ*, 715, 1508
Steinmetz M., 1996, *MNRAS*, 278, 1005
Sun M., Voit G.M., Donahue M., Jones C., Forman W., Vikhlinin A., 2009, *ApJ*, 693, 1142
Sunyaev R.A., Zeldovich Y.B., 1972, *Comments on Astrophysics and Space Physics*, 4, 173
Thomas P.A., et al., 1998, *MNRAS*, 296, 1061
Tormen G., Bouchet F.R., White S.D.M., 1997, *MNRAS*, 286, 865
Tornatore L., Borgani S., Dolag K., Matteucci F., 2007, *MNRAS*, 382, 1050
Tornatore L., Borgani S., Viel M., Springel V., 2010, *MNRAS*, 402, 1911
Tozzi P., Norman C., 2001, *ApJ*, 546, 63
Vazza F., Brunetti G., Gheller C., Brunino R., 2010, *New Astronomy*, 15, 695
Vikhlinin A., 2006, *ApJ*, 640, 710
Vikhlinin A., Markevitch M., Murray S.S., Jones C., Forman W., Van Speybroeck L., 2005, *ApJ*, 628, 655
Vikhlinin A., Kravtsov A., Forman W., Jones C., Markevitch M., Murray S.S., Van Speybroeck L., 2006, *ApJ*, 640, 691
Vikhlinin A., et al., 2009, *ApJ*, 692, 1033
Voit G.M., 2005, *Reviews of Modern Physics*, 77, 207
Voit G.M., Kay S.T., Bryan G.L., 2005, *MNRAS*, 364, 909
Werner N., Durret F., Ohashi T., Schindler S., Wiersma R.P.C., 2008, *Space Sci Rev*, 134, 337
Wiersma R.P.C., Schaye J., Smith B.D., 2009, *MNRAS*, 393, 99
Wiersma R.P.C., Schaye J., Dalla Vecchia C., Booth C.M., Theuns T., Aguirre A., 2010, *MNRAS*, 409, 132
Wurster J., Thacker R.J., 2013, *MNRAS*, 431, 2513
Zhang Y.Y., Böhringer H., Finoguenov A., Ikebe Y., Matsushita K., Schuecker P., Guzzo L., Collins C.A., 2006, *A&A*, 456, 55
Zhang Y.Y., Laganá T.F., Pierini D., Puchwein E., Schneider P., Reiprich T.H., 2011, *A&A*, 535, A78